SPECIAL COMMUNICATION

Foresail-2: Space Physics Mission in a Challenging Environment

Marius Anger[1] · Petri Niemelä[1] · Kiril Cheremetiev[1] · Bruce Clayhills[1] ·
Anton Fetzer[1] · Ville Lundén[1] · Markus Hiltunen[1] · Tomi Kärkkäinen[1] ·
M. Mayank[1] · Lucile Turc[2] · Adnane Osmane[2] · Minna Palmroth[2,3] ·
Emilia Kilpua[2] · Philipp Oleynik[4] · Rami Vainio[4] · Pasi Virtanen[4] ·
Petri Toivanen[3] · Pekka Janhunen[3] · David Fischer[5] ·
Guillaume Le Bonhomme[1] · Andris Slavinskis[6] · Jaan Praks[1]

Abstract

Earth's radiation belts are extremely important for space weather because they can store and accelerate particles to relativistic energies, which can have a potential impact on satellite functionality, communications, and navigation systems. The FORESAIL consortium wants to measure these high-energy particle fluxes to understand the dynamics of the radiation belts with its satellite mission Foresail-2. The mission aims to measure magnetic ultra low frequency waves and the plasma environment in the magnetosphere around Earth. The captured data will help to improve our understanding of space weather, and in particular the dynamics of Earth's radiation belts during periods of large disturbances inside the magnetosphere. A mission design analysis and several trade-off studies are conducted to find the requirements for the science payloads and spacecraft avionics design. Deducted from these requirements, four different payloads are proposed to gather science data in a highly elliptical orbit such as a geostationary transfer orbit. The precision magnetometer uses flux-gate technology to measure magnetic waves from 1 mHz to 10 Hz. The spin scanning particle telescope is built around a detector stack to measure electron spectra in the range of 30 keV to 10 MeV. Additionally, this mission serves as a technology demonstrator for the Coulomb drag experiment which proposes a new kind of electric solar wind sail utilising the Coulomb drag force imposed onto a 300 m long tether. The fourth payload investigates multilayer radiation shielding and single event effects. All payloads will be supported by a newly developed 6U platform using mostly commercial off-the-shelf components. Its proposed avionics face several unique design requirements rising from the payloads and the preferred highly elliptical orbit for this mission.

Note by the Editor: This is a Special Communication. In addition to invited review papers and topical collections, Space Science Reviews publishes unsolicited Special Communications. These are papers linked to an earlier topical volume/collection, report-type papers, or timely papers dealing with a strong space-science-technology combination (such papers summarize the science and technology of an instrument or mission in one paper).

Extended author information available on the last page of the article

1 Introduction

Even though Earth's radiation belts have been extensively studied since their discovery in the 1950s, our understanding of the variability of high-energy particle fluxes in this region remains largely incomplete (Ripoll et al. 2020; Vainio et al. 2009; Lejosne et al. 2022; Allen et al. 1958). Earth's radiation belts comprise an outer belt, populated by relativistic electrons, and an inner belt where both high-energy protons and electrons are found. These belts are separated by a slot region, which is mostly devoid of particles (Van Allen and Frank 1959). Typically, the outer belt extends between 12,000 km and 60,000 km above Earth's surface, thus encompassing the geostationary orbit, and the highest particle fluxes are found between 20,000 km to 30,000 km. While the inner belt is relatively stable, the intensity of particle fluxes in the outer radiation belt varies on timescales from minutes to days in response to solar wind driving and geomagnetic activity (e.g. Baker et al. 2019). Observations show that the fluxes of energetic particles can increase dramatically or drop suddenly by several orders of magnitude, within time scales of less than one day, and sometimes much shorter (Thorne 2010). Furthermore, the positions of the outer belt and the slot region are not constant in time, as for example the slot region can be filled with energetic particles during extreme events (Blake et al. 1992; Baker et al. 2013).

The radiation belts play a central role in causing adverse space weather conditions in near-Earth space. Enhancements in the high-energy particle fluxes, for example during magnetic storms, affect spacecraft passing through the radiation belts and can significantly impact the operational lifetime of satellites in orbit (Koons and Fennell 2006). Accurate models are required for satellite manufacturers and operators to make appropriate design decisions and to ensure the durability and resilience of the spacecraft. This calls for a thorough understanding of radiation belt dynamics, particularly the physical processes governing the energetic particle fluxes.

In recent years, significant progress has been made in radiation belt physics thanks to the data collected by NASA's twin Van Allen probes (Baker et al. 2019; Ripoll et al. 2020). However, the relative importance of the different acceleration and loss mechanisms at play remains unclear (Baker et al. 2018; Ripoll et al. 2020; Lejosne et al. 2022). More data are needed to unravel the physical processes at play further. With the end of the Van Allen Probe mission in 2019, there is no longer continuous monitoring of the radiation belts in the equatorial plane apart from data acquired by satellites in geostationary orbit. As the solar cycle approaches its maximum (expected in 2024-2025), a new mission targeting the radiation belts would be extremely timely, to investigate the response of the radiation belts during periods of intense geomagnetic activity, thus complementing the dataset from the Van Allen probes which were operated during a mild solar cycle.

Though CubeSat missions have been mostly limited to Low Earth Orbit (LEO), where radiation levels are modest, small satellites are proposed to be deployed in highly elliptical orbits such as the Geostationary Transfer Orbit (GTO) to conduct more in-depth space weather observations (Madry and Pelton 2020; Kopacz et al. 2020). Such highly elliptical orbits present several challenges that need to be overcome when designing successful missions:

At the apogee, the communication distances are at least 20 times longer than on LEO. In combination with the need to send several MB per day and the limited power resources of a CubeSat, a sophisticated communication solution is needed. As the orbital period of such orbits is typically several hours and the spacecraft is most of the time near the apogee, system thermals have also to be considered in detail. A thermal analysis will not be made in this article as a study is currently in progress for the shown spacecraft design.

Additionally, the injection into a GTO-like orbit has high lifetime uncertainties, which can lead to orbital lifetimes reaching from weeks to tens of years depending on the launch time and day (Lamy et al. 2012; Wang et al. 2020).

Furthermore, the flux of ionising radiation is increased in comparison to LEO due to trapped particles in Earth's magnetic field (Russell 2000). As the spacecraft passes through the high radiation region, a radiation mitigation strategy is needed to protect the commonly used Commercial Off-The-Shelf (COTS) components (Winokur et al. 1999; Nasa 1996).

The Finnish Centre of Excellence in Research of Sustainable Space (FORESAIL) wants to demonstrate the capability of small satellites to perform science missions in high elliptical orbits under these extremely challenging conditions.

This article presents the mission and spacecraft design of the Foresail-2 (FS2) CubeSat to study Earth's radiation belt regions. Firstly, the scientific motivation for this mission is discussed in Sect. 2. This results in the requirements needed to conduct the mission (Sect. 2.6). In Sect. 3 the derived payloads are discussed. The resulting mission and spacecraft design are explained in Sect. 4. Furthermore, a brief comparison with other missions is given in Sect. 5.

2 Motivation

The FS2 mission aims to improve our understanding of radiation belt particle dynamics in response to Ultra Low Frequency (ULF) waves, by providing a new set of measurements in this region. ULF waves in the inner magnetosphere have major importance for the dynamics of the outer radiation belt (Elkington 2006). Thus, quantifying their impact on relativistic electron fluxes is crucial.

The FS2 mission will concentrate on two types of ULF waves which are routinely observed in the magnetosphere and have been shown to strongly affect radiation belt electrons: ULF waves in the Pc5 frequency range and Electromagnetic Ion Cyclotron (EMIC) waves.

2.1 Ultra Low Frequency Waves in the Pc5 Range

Continuous pulsation (Pc) range fluctuations in the Pc5 frequency band (2 mHz to 7 mHz, see for example Glaßmeier 2007) are routinely observed inside Earth's magnetosphere (e.g. Anderson et al. 1990; Liu et al. 2009; Murphy et al. 2020; Sarris et al. 2022). A large fraction of these waves is caused by processes occurring outside the magnetosphere, for example, fluctuations in the solar wind dynamic pressure in the same frequency range or surface waves at the magnetopause which trigger oscillations on Earth's magnetic field lines (e.g. McPherron 2005; Menk 2011). Parts of these waves are also generated internally, due to local plasma instabilities, generally during disturbed times such as magnetospheric substorms and magnetic storms (e.g. McPherron 2005; Menk 2011). Compressional Pc5 wave power tends to be stronger on the dayside, near the outer boundary of the magnetosphere, while transverse fluctuations in the azimuthal direction, associated with standing waves on Earth's magnetic field lines, are observed across all magnetic local times (MLTs) (e.g. Sarris et al. 2022). The Pc5 wave power strongly depends on solar wind driving and tends to increase with increasing solar wind velocity and density or pressure variations (Liu et al. 2010; Takahashi et al. 2012; Bentley et al. 2018). Pc5 wave activity is also strongly enhanced during geomagnetic storms (Kalliokoski et al. 2020; Mathie and Mann 2001; Nikitina and Trichtchenko 2021; Sandhu et al. 2021).

Pc5 ULF waves are central to radiation belt dynamics because their periods are comparable to the drift periods of relativistic electrons around the Earth. As a result, energy exchange can take place between the waves and the particles through resonant interactions. Pc5 waves cause in particular inward and outward radial transport of electrons that can lead to an increase of particle energies or to their losses at the magnetopause (Jaynes et al. 2018; Lejosne and Kollmann 2020; Turner et al. 2012; Brito et al. 2020). On timescales shorter than the drift period, narrowband coherent Pc5 waves can cause drift-resonant acceleration of radiation belt electrons, which appears as oscillations in the particle fluxes at the same period as the ULF waves (Elkington et al. 2003; Claudepierre et al. 2013). On long timescales, much longer than the electron drift period, the accumulated effect of the interaction between the electrons and the ULF waves leads to radial diffusion (Lejosne and Kollmann 2020).

2.2 Electromagnetic Ion Cyclotron Waves

Electromagnetic Ion Cyclotron (EMIC) waves, with frequencies in the Pc1–2 ULF range (0.1 Hz to 5 Hz), are discrete electromagnetic emissions caused by temperature anisotropies in the ring current ion populations (e.g. Fraser et al. 2006; Usanova et al. 2016). They can be generated in multiple distinct bands, associated with the gyro frequency of the resonant ion population (e.g. H^+ band, He^+ band). Their source is thus internal to the magnetosphere, and their occurrence rate, their properties and their spatial distribution strongly depend on the solar wind conditions and the level of geomagnetic activity (Saikin et al. 2016; Chen et al. 2019; Jun et al. 2021).

The majority of EMIC wave events are observed during the recovery phase of geomagnetic storms (Saikin et al. 2016). Sheath regions preceding interplanetary coronal mass ejections can also lead to enhanced EMIC wave activity (Kalliokoski et al. 2020). The occurrence rate of EMIC waves is larger on the dayside, with generally a peak in the afternoon sector (Min et al. 2012; Saikin et al. 2015; Chen et al. 2019; Jun et al. 2021; Sigsbee et al. 2023). H^+ band EMIC waves tend to be found mostly outside the plasmasphere, while waves in the He^+ band are observed predominantly inside the plasmasphere (Jun et al. 2021). Multi-spacecraft observations suggest that the extent of individual EMIC wave events ranges between 0.5 h to 3 h in MLT, with larger extents found on the dayside (Clausen et al. 2011; Blum et al. 2017).

EMIC waves are important for the radiation belt dynamics, as they precipitate efficiently relativistic electrons ($> \sim$ MeV) via pitch angle scattering. However, many open questions remain regarding their impact on particle precipitation in the upper atmosphere. For example, it is still unclear whether they can also induce precipitation of particles in the sub-MeV range (Denton et al. 2019; Ripoll et al. 2020). Characterising the spatial extent and the duration of EMIC events is crucial to accurately quantify their contribution to electron losses.

2.3 Science Questions and Objectives

The following science objectives were identified for the Foresail-2 mission:

2.3.1 S1: What Is the Role of ULF Waves in Accelerating, Transporting, and Scattering of Electrons in Earth's Radiation Belts as a Function of Solar Wind Driving and Magnetospheric Activity?

S1.1: Quantify the role of magnetospheric activity, Pc5 and EMIC ULF waves for the response of the radiation belt electrons (e.g., increase, depletion, or no change in the particle

fluxes, modification of the pitch-angle distribution, evolution of the phase space density) over a wide range of energies and locations as a function of solar wind structures (e.g., during coronal mass ejection ejecta and sheaths, stream interaction regions and fast streams) and magnetospheric activity.

S1.2: Explore the impact of solar wind drivers and magnetospheric activity on the ULF Pc5 and EMIC (2 mHz to 5 Hz) wave properties.

S1.3: Integrate the Foresail-2 data with measurements by other spacecraft in the solar wind and magnetosphere, as well as from ground-based facilities to resolve whether waves are externally transferred or internally generated (substorm activity).

S1.4: Characterise the response of electrons to ULF waves (e.g., increase, deplete or have no change at all).

2.3.2 S2: How do ULF Waves and Turbulence Transmit Within the Inner Magnetosphere?

S2.1: Study the variation of wave properties, such as frequency spectra, polarisation, correlation lengths, etc., from ULF frequencies upwards to turbulent frequencies as these waves travel within the inner magnetosphere.

S2.2: Characterise the spatial variation of wave properties in the largest range of L-shells and magnetic local time as possible, by having the spacecraft reach a wide range of locations in near-Earth space.

S2.3: Investigate the temporal variations of the wave properties as a function of solar wind driving conditions.

2.4 Technology Demonstrators

In addition to scientific goals, FORESAIL also wants to deliver unique testing capabilities to promote new technologies. The following technologies are considered during this mission design study.

2.4.1 Coulomb Drag

Coulomb Drag (CD) has been proposed for interplanetary transportation in the form of an Electric Solar Wind Sail (E-Sail) in the solar wind or a Plasma Brake (PB) for de-orbiting within LEO (Janhunen 2004; Janhunen and Sandroos 2007; Janhunen et al. 2013). The E-Sail and PB interact with the natural plasma stream such as solar wind or ionospheric ram flow via long and charged tethers to transfer momentum to the spacecraft. The PB capabilities of this technology will be demonstrated by Foresail-1p and ESTCube-2 (Iakubivskyi et al. 2020).

Additionally, the plasma density can be estimated with the tether, as the electron current gathered by the positive tether depends on the density of the surrounding plasma. In principle, the drag can be measured for vastly different plasma densities from the dense ionospheric plasma (starting from ~ 90 km) to the tenuous plasma outside the plasmasphere (~ 4 Earth radii).

2.4.2 Radiation Shielding

Despite the interest in the radiation belts, current commercial CubeSat platforms cannot tolerate the radiation levels encountered there (Madry and Pelton 2020). Most COTS components remain operational after 5 krad of ionising dose, while some have been observed to

function after more than 20 krad (Sinclair and Dyer 2013). Sensitive components must be shielded to reduce the Total Ionising Dose (TID) they receive to a level at which they can be expected to operate without failures.

Radiation shielding for CubeSats is an optimisation problem due to the size and mass limitations of the satellite standard. Previous work for the FORESAIL project identified multilayer shielding material candidates for a CubeSat mission on GTO and the corresponding publication is under review (Fetzer et al. 2023b). Monte Carlo particle transport simulations using Geant4 (Agostinelli et al. 2003; Allison et al. 2006, 2016) were performed to estimate the ionising dose deposited behind shielding by particle spectra predicted using space radiation models available on SPENVIS (Donder et al. 2018). Conservative multilayer shielding recommendations have been derived, which would keep the long-term average dose rate inside the spacecraft below 1 krad per month (Fetzer 2023a,b,c). In-situ measurements are needed to verify the actual ionising dose rates and TID behind the proposed radiation shield and to demonstrate that COTS components can be operated on GTO inside a CubeSat for the proposed mission duration of 6 months.

2.5 Technology Objectives

The following questions and objectives have been derived from the technology demonstrators on this mission.

2.5.1 T1: How Does the CD Force Depend on the Surrounding Plasma Parameters and the Tether Voltage?

T1.1: Characterise the relationship between the CD force and plasma density in various plasma environments - starting from the ionosphere to the outside of the plasmasphere to understand the effectivity of PB and E-Sail devices.
T1.2: Closely study the relationship between the CD force and the tether voltage to identify the system requirements for future missions.

2.5.2 T2: Can CubeSats Use COTS Components in the Radiation Belts?

T2.1: Compare the measured and simulated TID rates for several shielding material combinations to verify the results with in-situ spectra.
**T2.2:** Study the severity of SEEs to derive mitigation requirements for missions in highly elliptical orbits.

2.6 Measurement and Instrument Requirements

In order to answer the science questions the mission shall provide magnetic field, energetic particle flux and plasma density measurements.

To effectively use the CD force a tether has to be extended from the satellite and used for drag measurements and as a scientific plasma instrument. Radiation tolerance testing requires low-duty-cycle measurements for TID experiments and continuous SEE monitoring.

Figure 1 illustrates the dependency of each measurement requirement (OR) on the science and technology objectives (S and T).
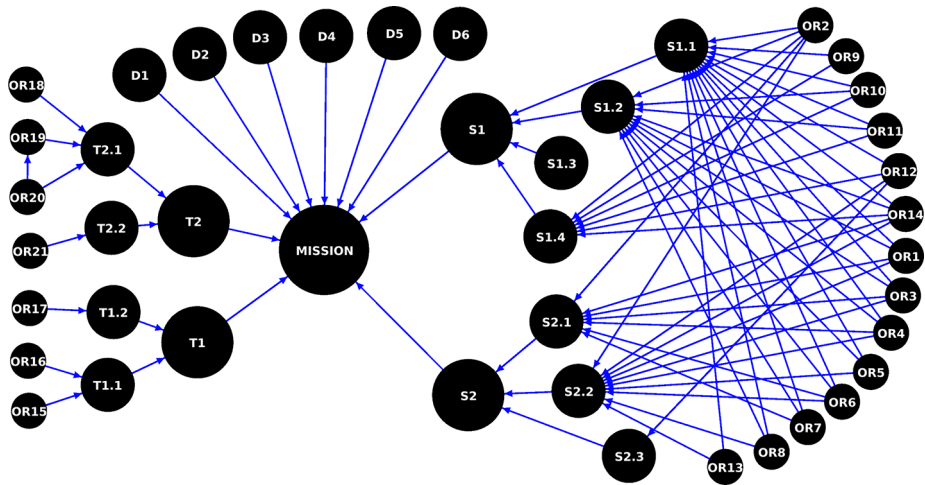
Fig. 1 Requirement dependencies for the Foresail-2 measurement requirements (OR). Detailed information about each requirement is provided in the accompanying text

2.6.1 Magnetic Field

To address Science Questions S1.1, S1.2, S2.1 and S2.2 the magnetic field vector shall be measured in a frequency range of 1 mHz to 10 Hz with a minimum sampling frequency between 1-2 Hz for Pc5 waves and of at least 10 Hz (OR4, OR5). The sampling frequency is determined by the waves of interest with the highest frequencies, namely the EMIC waves. These waves have frequencies between 0.1 Hz and 5 Hz, which requires a sampling rate of at least 10 Hz. The waveforms will be barely resolved with a 10 Hz sampling rate, with only two data points per wave period. A higher sampling rate will enable resolving the waveforms with greater accuracy. The magnetic field magnitude shall be observed in the range from 0.1 nT to 1000 nT (OR6). The maximum acceptable noise levels are 1 nT^2/Hz for 1 mHz waves and 10^{-3} nT^2/Hz for 1 Hz waves (OR7, OR8). These noise levels have been determined based on the ULF wave power measurements by the GOES satellites. A statistical study showed that the average quiet time levels of Pc5 wave power are of the order of 5 nT^2/Hz, while the average wave power in the EMIC band is around 10^{-3} nT^2/Hz (Kalliokoski et al. 2020). The selected noise level enables measuring Pc5 waves both during quiet times and storm times, as these waves are routinely encountered inside the magnetosphere. EMIC waves on the other hand mainly occur during storm times (Saikin et al. 2016), so the threshold was set in order to capture waves at storm-time levels, which are most relevant for our science objectives.

To aid the science objective S1.2, the magnetic field intensity should be measured in the Pc5 frequency range (2 mHz to 7 mHz) with a noise level of 50 nT^2/Hz for 2 mHz, but preferably better.

2.6.2 Energetic and Relativistic Electrons

To satisfy objectives S1.1 and S1.4, measurements of the electron energy spectrum shall cover 800 keV to 8 MeV along 12 lines of sight at a given time (15° angular resolution) (OR9).

The ULF wave-particle interactions with 100 keV to 1000 keV result in drift-resonant and non-resonant responses in the fluxes (e.g. drift echoes, zebra stripes). Signatures of ULF wave-particle interactions have been measured for decades (Kokubun et al. 1977; Claude-pierre et al. 2013), but in order to distinguish drift-resonant and non-resonant responses in the fluxes one requires an energy resolution that is sufficiently fine (Hartinger et al. 2020; Osmane et al. 2023). With an energy resolution $\Delta E/E$ of 20% a ULF wave with moderate amplitude (less than a few nT), that resonates with 500 keV equatorially trapped electrons (19.5 drift period at L-6), should not resonate with a 400 keV electron (23.5 s drift period). The 400 keV electron will nonetheless experience a lower-amplitude non-resonant modulation (drift-echo). For EMIC wave-particle interactions, the resonant energies for 1 to several MeV electrons are highly dependent on the plasma ions density ratio (i.e. between hydrogen and helium ions or/and hydrogen and oxygen ions) (Summers and Thorne 2003). For typical plasmaspheric conditions, the threshold for efficient EMIC wave scattering can start from 800 keV to several MeV. With a resolution of $\Delta E/E$ of 100% it is possible to distinguish the energy range where losses driven by EMIC waves are taking place.

Therefore, below 1000 keV, the energy resolution $\Delta E/E$ shall be at 20% (OR10). In the 1 MeV to 8 MeV range, an energy resolution $\Delta E/E$ of 100% shall be provided (OR11). The range could be extended to 30 keV to 10 MeV along 30 lines of sight at a given time (6° angular resolution) with an energy resolution $\Delta E/E$ of 20% to resolve smaller population differences.

2.6.3 Electron Density

For S1.1, S1.4 and S2.2, electron density measurements shall be done with a one-minute temporal resolution to determine if the spacecraft is inside or outside the plasmasphere (OR12). Such distinction can be determined by estimating more than an order of magnitude difference in the electron density – inside the plasmasphere, it is between 10^2 and 10^3 particles per cm^3, and outside the density is below 10 particles per cm^3 (OR13).

This information is important for the scientific objectives as ULF wave properties differ inside and outside of the plasmasphere (Liu et al. 2011; Takahashi et al. 2010; He et al. 2020), and the measurements will therefore provide crucial context to interpret the magnetic field measurements.

Additionally, the electron density measurements should be performed at high temporal resolution (up to one second in high-density plasma environment) to observe density fluctuations of the order of one particle per cm^3 in the 1 mHz to 1000 mHz range, which are associated with compressive ULF waves.

2.6.4 Coulomb Drag Force

The CD force (T1.1) is estimated by measuring the changes in the spin rate of the satellite. Observations with different tether voltages and lengths shall be performed to satisfy T1.2. A force of 0.1 nN per meter of tether length (conservative assumption) introduces a $\sim 1.6°$ difference in the phase angle when integrated over an hour and assuming a 300 m aluminium tether(OR17). Thus, the attitude resolution shall be at least 1°/h with an accuracy of at least 2° (OR15). Such a tether weighs 3.3 g, with the required tether tip mass adding ~ 2.5 g.

2.6.5 Radiation

The actual dose accumulated by the onboard electronics shall be measured with enough relative and temporal resolution to monitor the TID accumulation over the mission duration (T2.1). Due to the dynamics of the radiation belts, the received particle flux rates are

expected to fluctuate on time scales of less than a day, as shown in Sect. 1. Assuming a long-term average dose rate inside the shielded volume of the spacecraft of less than 1 krad per month, a precision better than 30 rad shall be provided to resolve the average daily dose accumulation (OR18).

To verify previous shielding simulations, the ionising doses behind thinner aluminium shielding and alternative shielding materials shall be measured with a relative resolution better than 1% (OR19). The expected relative performance differences between alternative materials are larger than 10% as concluded from simulations with Geant4 (Fetzer 2023a,b,c,d,e). Assuming a long-term average dose rate of 1 krad per month and one month of integration time, this results in an absolute precision of 10 rad (OR20).

To study SEEs, monitoring functionality shall be implemented for a component that typically experiences SEEs (OR21). As the susceptibility to SEEs and the impact of SEEs is dependent on the chip structure and architecture, only chip-specific conclusions can be made.

2.7 Mission Requirements

The following mission requirements have been identified according to the science objectives and the measurement requirements. These will form the demands for the launcher, space and ground segments.

Orbit: The orbit for this mission shall pass through both radiation belts frequently to satisfy S2 and S1 (OR1, OR2). A inclination of $< 30°$ is needed for the scientific objectives of the mission (OR3): The spacecraft's orbit needs to lie near the equatorial plane in order to measure those electrons whose mirror points are close to the equator. At higher latitudes, the spacecraft would only measure the part of the high-energy electron population that has its mirror points at higher latitudes. This low inclination is comparable to that of other radiation belt missions such as the Van Allen Probes and the Arase satellite.

To ensure control authority from Finland, the satellite's ground track and communication schedule shall be optimized for visibility from Finnish ground stations.

Launch date: To perform measurements during high solar activity, which is especially interesting for wave propagation science, the launch shall occur in late 2024 or the beginning of 2025.

Attitude: To facilitate the calibration of onboard magnetometers and to provide the scanning ability for particle measurements, the spacecraft shall spin with a period of 10 s to 20 s and maintain the spin axis perpendicular to the local magnetic field direction. For conducting magnetometer calibration and scanning the surrounding plasma in a controlled manner, the attitude control accuracy shall be at least 2° or better. The attitude shall be known with a precision of 1° to achieve the proposed resolution for electron and magnetic field measurements. To deploy the CD tether an angular momentum of approximately 21 N m s shall be provided by the spacecraft.

Lifetime: To yield sufficient data the mission shall have an orbital lifetime of at least 6 months (OR14). This ensures a measurement of at least one geomagnetic storm. Ideally, several storms would occur during this time period. Additionally, an orbital lifetime of below 25 years shall be maintained. Preferably, the lifetime is below 5 years to minimize space debris as much as possible.

Duty cycle: The magnetic measurements shall be active at least in the outer radiation belt to cover S2.2 (OR1). Particle detection should only be conducted inside the plasma (OR2). The CD force shall be measured 100% of the orbital period to accurately determine the small forces involved (OR16).

2.8 Project Drivers

In addition to requirements, other project drivers need to be considered that do not arise from science questions or technology objectives. These drivers do not affect the mission requirements but rather influence the solutions to fulfil those requirements.

CubeSat heritage and available budget (D1): The platform provider (Aalto University) as well as some of the science instrument providers have conducted missions together in the past. On the first Finnish satellite, Aalto-1, which was launched in June 2017 into LEO and is still operational, a plasma brake demonstrator by FMI as well as the radiation monitor RAD-MON by the University of Turku are flying as payloads (Gieseler et al. 2020; Mughal et al. 2021; Praks et al. 2021). In 2021 the 3U Foresail-1 (FS1) satellite was launched into LEO as part of the FORESAIL project (Palmroth et al. 2019). Its payloads are a particle scanning telescope called PATE and a plasma brake technology demonstrator (Gieseler et al. 2021). Due to an operational error, the satellite did not enter its science mission. A second satellite Foresail-1p (FS1p) is currently under development. Considering the available technologies and budget, the mission should obey the CubeSat standard (Poly 2022).

Education of future Finnish satellite builders (D2): The platform is intended to serve educational purposes for students interested in space technology and satellites, with a focus on hands-on experiences.

Finnish CubeSat science platform (D3): The platform may also aid future missions of the Finnish science community.

3 Instrumentation

The FS2 satellite has three main instruments: Magnetometer Aboard the ForeSail-2 cubesaT (MAST), developed by the Austrian Space Research Institute, Relativistic Electron and Proton Experiment (REPE) by the University of Turku and Coulomb Drag Experiment (CDE), developed by the Finnish Meteorological Institute. In addition, a small Radiation Experiment (RadEx) is developed by Aalto University.

3.1 Magnetometer Aboard the ForeSail-2 CubesaT (MAST)

MAST is a miniaturized version of the fluxgate magnetometer technology used for the FIELDS instrumentation suite on the Magnetospheric Multiscale mission, designed to measure the magnetic field in Earth's magnetosphere (Torbert et al. 2016). The implementation used on FS2 is a new development, which employs a newly developed 4th-generation Magnetometer Frontend Application-specific integrated circuit (MFA) (Auer et al. 2018).

Fluxgate magnetometers measure the magnetic field by driving a highly permeable core to saturation using a periodic drive current through the drive coil. The resulting magnetic field exhibits a nonlinear relation to the current, as it changes along the nonlinear magnetisation curve of the core. This field is measured using a secondary coil (the sense or pickup coil). The measured signal consists of the fundamental drive frequency, its odd harmonics generated by core saturation as well as additional even harmonics generated by external fields.

A fluxgate is not an absolute instrument. Scale factor and offset values depend on the implementation and require calibration relative to an absolute magnetic field calibration source.

Fig. 2 Fluxgate sensor head of MAST at the tip of the FS2 twofold boom with the cover dome removed
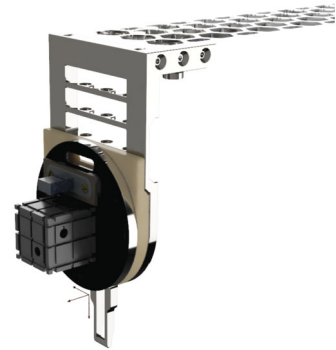
Table 1 REPE instrument target performance for electrons and protons

Particle species	Energy range [MeV]	Energy resolution [%]
Electrons	0.4-8	20 for < 1 MeV
		50 for > 1 MeV
Protons	5-500	30

The drive signal is provided using a Metal-Oxide Semiconductor Field-Effect Transistor (MOSFET) switch supported by passive components (inductors and capacitors). Measurements and feedback are conducted using Analog-to-Digital and Digital-to-Analog Conversion (ADC/DAC), controlled by a regulation loop in an FPGA. This FPGA is also responsible for interface handling, packaging, housekeeping measurements, and handling auxiliary magnetometers. It uses an RS-485 interface for communications with the satellite.

As seen in Fig. 2, the fluxgate sensor itself is mounted on a boom and is connected to the electronics with a harness. The instrument needs 2.5 W of power when active in science mode. The measurement head has a weight of 120 g and rough dimensions of $5.4 \times 5.4 \times 2.8$ cm^3 so that it can fit into the tuna can volume. Whereas the electronics box inside the satellite fits into $14.6 \times 8.4 \times 3$ cm^3 and weighs around 400 g. The boom increases the distance between potential magnetic disturbance sources and the sensor, which also decreases the magnitude of the disturbances at the sensor position. MAST employs an additional, low-sensitivity magnetometer that is used to measure the magnetic field of dynamic disturbance sources within the satellite. This information can be used to identify and model magnetic disturbance sources that are significantly closer to the inner magnetometer than MAST. For monitoring the total ionising dose on the frontend MFA, MAST utilises a RADiation-sensitive metal-oxide-silicon Field-Effect Transistor (RADFET).

3.2 Relativistic Electron and Proton Experiment (REPE)

REPE will measure electrons and protons count rates and energies with a particle telescope stack (Oleynik et al. 2023). The targeted energy ranges and energy resolutions of the instrument are given in Table 1.

The instrument has a collimated aperture followed by a relatively thick window of 200 μm aluminium that eliminates the lowest energies from the measurements (shown in Fig. 3). The instrument fits into an envelope of $9 \times 7.6 \times 9.5$ cm^3 and weighs around 1000 g.

The first detector layer (D1) is a $2.1 \times 2.1 \times 0.35$ mm^3 Si detector, the second one (D2) is a $5.0 \times 5.0 \times 0.35$ mm^3 Si detector, the third one (D3) is a $10 \times 10 \times 10$ mm^3 scintillator

Fig. 3 Mechanical model of the REPE instrument on board the FS2 satellite: On the left, a sliced view is shown. The right shows the measurement slit on the front of the instrument. It fits into $9 \times 7.6 \times 9.5$ cm^3
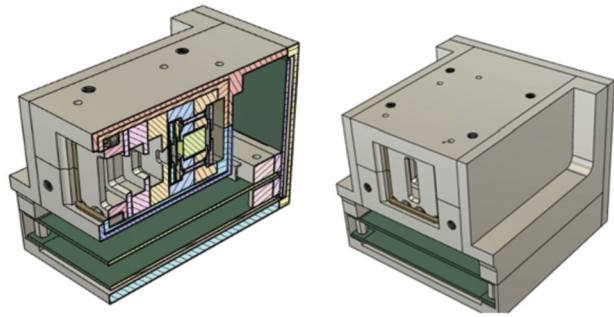
Fig. 4 Coulomb Drag Experiment in the FS2 version with electron emitter and 300 m long tether. Its envelope is $9.5 \times 8.4 \times 13$ cm^3

made of GAGG (Gd$_3$Al$_2$Ga$_3$O$_{12}$) and readout with a photodiode or a Si photomultiplier, and the fourth one (D4) is a $10 \times 10 \times 0.35$ mm^3 Si detector.

A hit from D1 is required only if D3 (and D4) are not hit. Once there is a hit from D3, D1 pulse height is no longer used in the analysis, and the geometric factor of the instrument thus increases by a factor of 5.5 in the ratio of the detector areas, thus allowing lower fluxes to be measured in accordance with the spectrum in the environment. In very high flux conditions, detection thresholds can be elevated to avoid saturation, and the lowest energies (< 0.8 MeV) can be eliminated entirely from the electron spectrum. In full science mode REPE can draw up to 2.5 W.

3.3 Coulomb Drag Experiment (CDE)

As a high elliptical orbit provides a wide variety of plasma conditions, the Coulomb Drag Experiment (CDE) includes both negative and positive polarity High Voltage (HV) systems. The negative mode is employed at perigee as a PB, while the positive mode is used around the apogee as an E-Sail. The mechanics and electronics of the experiment build on the heritage of payloads onboard Foresail-1 (PB) and ESTCube-2 (PB and E-sail) (Iakubivskyi et al. 2020). As these missions were designed to function in LEO, several design changes, improvements, and additions were introduced to the FS2 CDE payload.

The CDE consists of a motorised tether reel to deploy the tether, and two high-voltage sources (as seen in Fig. 4) that, when turned on, bias the deployed tether to nominally -1 kV, $+1$ kV, and $+0.5$ kV relative to the spacecraft chassis. The instrument weigths around 1000 g and has an envelope of $9.5 \times 8.4 \times 13$ cm^3. The conductive tether is 300 m and will be

Fig. 5 RadEx instrument on board the FS2 satellite with different materials in the top row and different aluminium thicknesses in the bottom row. It fits into $6.6 \times 2.6 \times 13$ cm^3
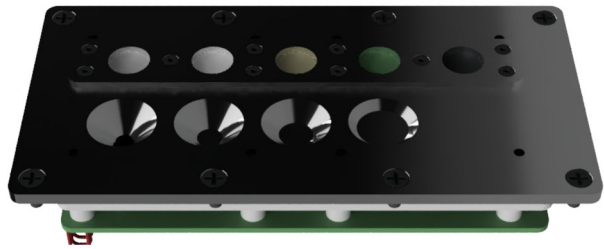
deployed in steps. It is possible to apply a high voltage to the tether also at intermediate tether lengths as the HV contact to the reel and tether is available through a slider contact throughout the deployment.

The PB mode biases the tether negatively (nominally to -1 kV) with respect to the surrounding plasma (Janhunen et al. 2013). The negatively charged tether collects positively charged ions from the plasma (mainly oxygen ions and protons). The conducting surface of the satellite, which includes its body as well as the boom, collects the same electron current.

The E-sail mode biases the tether to a positive potential, $+1$ kV and $+0.5$ kV. This implies that the positive tether potential gathers electrons from the ambient plasma. In order to maintain the positive bias, FS2 is equipped with an electron gun (Iakubivskyi et al. 2020; Tajmar 2012). In this case, the electric current is flowing the other way around. It goes from the tether via ambient plasma to the electron guns and through the gun cathode to the tether.

Ideally, the deployment of the tether should be observed with a camera to see the exact dynamics of the end mass in the early reel-out phase. During reeling the instrument can draw up to 7 W. While measurement are conducted only 0.6 W are needed.
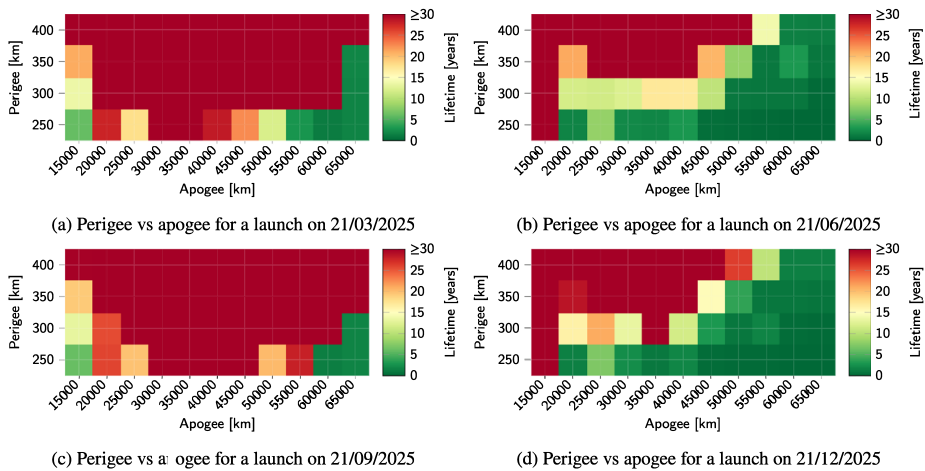
3.4 Radiation Experiment (RadEx)

RadEx will use RADFET TID sensors behind several different shielding configurations as shown in Fig. 5 (Fetzer et al. 2023a). The instrument fits into a volume of $6.6 \times 2.6 \times 13$ cm^3. With a top plate out of aluminium the instrument weighs around 400 g.

The 6 mm thick plate is part of the spacecraft shielding structure. It will have conical cutouts that leave different thicknesses of aluminium on top of the radiation sensors centred below the cutouts. One sensor will be exposed to space by a cutout that leaves no shielding material inside a 45° conical field of view above the sensor. Other sensors will be covered by 1 mm, 2 mm, 4 mm and the full 6 mm aluminium shielding. A second row of sensors will be covered by different material discs. Possible candidates are FR4, copper or stainless steel as well as multilayer shielding plates containing polyethylene and tantalum to measure the shielding performance of these alternative shielding materials. The thicknesses of the sample discs will be adjusted to result in the same shielding depth in g/cm^2.

The temperature of the RADFET sensors will be monitored closely to compensate for annealing.

Only the radiation sensors and radiation-insensitive components for example resistors and temperature sensors are going to be placed in the shielding cutouts with PCB traces carrying power and signals to and out of the high radiation area. The power distribution, switching, analogue to digital conversion and data processing will be done on a part of the PCB that is shielded by the full 6 mm of aluminium shielding. Additional shielding separates the sensor area from the rest of the spacecraft to prevent radiation from leaking to the other electronics inside.

(a) Perigee vs apogee for a launch on 21/03/2025

(b) Perigee vs apogee for a launch on 21/06/2025

(c) Perigee vs apogee for a launch on 21/09/2025

(d) Perigee vs apogee for a launch on 21/12/2025

Fig. 6 Perigee vs. apogee of simulated orbital lifetimes for FS2 6U CubeSat for four different launch dates (Anger 2023)

A microprocessor will be tested for its performance in an elevated radiation environment, especially regarding SEEs. This processor serves only to verify SEEs expectations and to test their severity. A second controller collects and processes the data of the radiation sensors and the microprocessor experiment.

Nominal operations of RadEx need up to 0.3 W.

4 Mission Design

With the mentioned instrumentation and the mission requirements the following design for the space segment has been envisioned. As this mission also serves as an educational platform (D2), most of the subsystems will be built from the ground up by the team at Aalto University, instead of buying them from industry.

4.1 Orbit

To satisfy the mission requirements OR1, OR2 and OR3 a minimum apogee of at least 15,000 km is needed for the FS2 mission. To cover both radiation belts a high eccentricity above 0.5 is desirable.

It has been shown that high elliptical earth-bound orbits exhibit drastic variations in orbital lifetime (Pons and Noomen 2019; Lamy et al. 2012; Wang et al. 2020). Therefore, a study is needed to find the best possible launch time to obey the lifetime regulations for satellites. Several different orbits from four potential launch dates were simulated with the European Space Agencies Debris Risk Assessment and Mitigation Analysis (DRAMA) tool around the equinoxes and solstices for a 14 kg satellite with an average surface area of 0.170 m^2 (Anger 2023).

The apogee height has been varied from 15,000 km to 65,000 km and orbits have been simulated for four different perigee heights from 250 km to 400 km. The results are shown for four different launch times in Fig. 6.

Almost all orbits up to GTO apogee heights and with a perigee higher than 300 km were not compliant with the 25 years guideline for a spacecraft without additional capabilities for deorbiting. With increasing apogee height the orbital lifetime is decreasing as seen in the performed simulations. Launches in spring and autumn were mostly not compliant with European guidelines. The orbital period ranges from 4.58 h to 21.35 h.

These simulations showed that even when launching in a well-defined orbit the time of the year plays a big role. Launches to highly elliptical orbits are rare and often do not offer space for ride-share options. Therefore, it widens the launch opportunities to include a deorbiting device. Currently, the best launch opportunities are available for GTO launches.

Even though the CDE can provide a method to deorbit the satellite even in a highly elliptical orbit, it has to be considered as a novel payload and as such has a higher failure risk than an already proven method. An additional system to deorbit the spacecraft after its science mission has to deliver at least 25 m/s of ΔV. This value is derived assuming a GTO orbit perigee height of 300 km that has to be lowered to a target disposal orbit perigee of 100 km and a 20% margin as well as the assumption that the manoeuvre is performed in apogee. This additional system ensures that a mission lifetime of below five years can be achieved, but the direct injection into an orbit with a low enough perigee height for a natural decay within the regulations has significantly lower risks due to the component degradation over the mission lifetime in this high radiation environment.
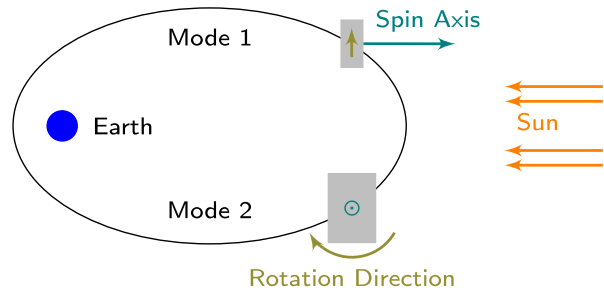
4.2 Attitude

Particular attention was given to the actuators in an Attitude and Orbit Control System (AOCS) trade-off study. The final configuration depends on the possibility of providing the required momentum for the tether deployment. The needed spin modes for REPE and MAST in addition to the power consumption and thereby the solar panel direction also have to be taken into account.

For all manoeuvres required by MAST and REPE a minimum total impulse of 5.8 N s is needed. The deployment of the CDE tether requires at least 19 spin-up manoeuvres with a summed minimum total impulse of 113.7 N s as it is deployed in steps to avoid too high forces on the tether. The later manoeuvres for the tether deployment require an increasing amount of angular momentum for the execution up to around 9500 mN m s as the inertial moment of the satellite spin axis increases due to the extending tether. These manoeuvres assume a spin around the body y-axis and a 6U CubeSat with 15 kg mass.

Magnetorquers cannot provide the required angular momentum even in best case simulations. They exceeded the manoeuvre time limit which was set by the science team. A design study with a reaction wheel unit revealed that especially for the tether deployment operation this type of actuator cannot be used. During one spin-up manoeuvre momentum dumping of the wheels is considered high risk as it may lead to uncontrolled tether tension. Typical CubeSat reaction wheels achieve up to 900 mN m s, thus cannot deliver the required angular momentum (Shields et al. 2017; CubeSpace 2023). Additionally, the spinning frequency of most reaction wheels on the market (up to 100 Hz (Shields et al. 2017; CubeSpace 2023)) is in the same region as the magnetic ULF waves and would introduce significant noise in the measurements. A propulsion-based attitude control system can provide the required angular momentum.

To obtain an estimate for the required thrust, manoeuvre time, and propellant mass, an analysis of different propulsion units was conducted (Bonhomme 2020). The electric propulsion units studied showed long manoeuvre times with very high average energy consumption of 1.2 kW h. In contrast, a cold gas-based propulsion system would require more propellant,

Fig. 7 Two possible spin-stabilised attitude configurations of Foresail-2 facing the sun. The spin axis is shown in teal and the rotation direction is shown in olive

which introduces its own attitude dynamics to the satellite structure. A hybrid system such as a resistojet system or a pure cold gas system is recommended due to the higher power demand of other systems. A detailed study of attitude control without reaction wheels has to be conducted.

The AOCS configuration should include a sun sensor for each of the six faces of the CubeSat. They shall act as the main attitude determination sensors and provide the desired accuracy. The use of a star tracker was discarded because its maximum limit on the tracking rate was in the order of 10° per second which is too slow for a spinning satellite. A three-axial magnetometer should provide information regarding the orientation of Earth's magnetic field in respect to the satellite at any point in the orbit. A Global Navigation Satellite Systems (GNSS) receiver will provide the position of the satellite in the inertial frame in order to compute the orbital velocity and position vectors of the slowly decaying orbit. Because the angular rates are one of the most important measurements, an Inertial Measurement Unit (IMU) composed of three gyros is to be accommodated in the AOCS set. At least two propulsion units will provide the means to deploy the tether, and a minimum of four propulsion units are needed in order to detumble the satellite. For deorbiting one thruster aligned with the centre of mass of the satellite is sufficient.

Based on the constraints collected from the major requirements, the mission design analyses, and the trade-off study on the AOCS configuration, five main pointing modes have been established: Safe Mode (SM), Coarse Pointing Mode (CPM), Tether Deployment Mode (TDM), and Orbit Maintenance and Deorbit Mode (OMDM).

Two possible attitude configurations for CPM and TDM (shown in Fig. 7) have been studied closer regarding the solar panel orientation and spin axis alignment.

The first mode points the satellite's Y axis towards the Sun. The satellite will rotate around the Y-axis to provide the required spin motion for the payloads. The orbit and attitude orientation will stay the same over the mission lifetime in relation to the Earth-Sun plane. Readjustments of the attitude towards the Sun are needed to deliver the same amount of solar energy to the solar panels at every stage of the mission. The second mode still rotates around the Y axis, but the axis is pointing perpendicular to the Earth-Sun plane. In this case, a readjustment of the rotational axis does not have to be performed. The solar panel configuration needs more cells and area than with the first mode.

The Attitude Determination System (ADS) will be built by the Aalto University team and consists of the proposed sensors and GNSS system. The IMU setup from previous missions can be reused. The GNSS receiver has heritage from Aalto-1 and is currently under development with the Aalto-3 student satellite mission (Praks et al. 2021). As the sun sensors from previous missions cannot sustain the elevated radiation environment on the surface of the satellite, they have to be bought. The current best candiadates are the Lens R&D Maus sun sensors (Leijtens 2021). The computing unit will use the same microcontroller as the OBDH

to simplify the development. It calculates all the necessary equations and algorithms. The propulsion-based Attitude Control System (ACS) has to be bought from an external supplier. Ideally, the ACS can be used for both use cases: attitude control and deorbiting. Based on GOMSpace NanoProp 6DOF such a module has a volume of less than 2U and a dry mass of around 700 g (GOMSpace 2020).

4.3 Radiation

A beyond-LEO orbit has not been used by CubeSats with a COTS components approach. The high-energy particles encountered in high orbits can cause damage to the onboard subsystems and lead to premature failures as well as the end of the mission if the spacecraft is not appropriately designed. Monte-Carlo particle tracking simulations with Geant4, as well as the analytical model SHILEDOSE-2, show that 6 mm of aluminium are sufficient to reduce the TID received by internal components of the spacecraft to less than 12 krad after one year in orbit (Fetzer et al. 2023b; Fetzer 2023a,b,c,d). These radiation levels inside the satellite allow the use of high-grade COTS components if additional measures are taken. Among others, error correction codes have to be implemented as the shielding cannot stop high-energy protons and ions. The satellite structure will provide radiation shielding to minimise double implementation. Payloads that have apertures are responsible for the shielding that may be required because of their openings.

4.4 Boom and Magnetic Cleanliness

As stated in Sect. 2.6.1 the measurement of ULF magnetic field waves needs a low magnetic noise environment for the precision magnetometer payload (MAST). The static magnetic interference at the reference point, the magnetometer mounting point, is required to stay below 35 nT, but preferably should be as low as possible. Currently, a level below 10 nT seems achievable. The dynamic magnetic interference from the spacecraft at the reference point should be lower than the $1/f$ noise limit with 0.707 nT/$\sqrt{\text{Hz}}$ at 1 mHz and 0.707 pT/$\sqrt{\text{Hz}}$ at 1 Hz. In addition, at 1 Hz to 10 Hz the spectrum should stay below 0.707 pT/$\sqrt{\text{Hz}}$.

A total magnetic emission budget has been determined for the spacecraft based on the maximum allowed net magnetic noise level. The total budget is a summary of the allocations for each subsystem, which specify the level of magnetic noise each system is allowed to induce at the reference point. From these allocations and the locations of each subsystem in the spacecraft, a maximum allowed Magnetic Dipole Moment (MDM) has been derived for each subsystem. The maximum MDMs are defined separately for static and dynamic fields. Based on the MDMs of all subsystems, two models to calculate the net magnetic interference at the reference point are considered: a worst-case scenario, and a model with a statistical tolerance to account for expected deviation in MDM orientations. The design choices are driven by the worst-case model.

To minimise the effect of magnetic disturbances originating from the spacecraft, the key mitigation technique is to spatially separate MAST from the magnetic emission sources of the spacecraft. For this purpose, a novel twofold deployable boom is under development to carry the magnetometer head. The deployment is observed via a sensor e.g. a camera.

The boom design is shown in an early design study in Fig. 8 which was performed at Aalto University. One focus is to enable cost-efficient manufacturing and easy mounting on a CubeSat. The minimum boom length that enables reaching the magnetic cleanliness requirements is 500 mm. Currently, the design achieves a separation of over 620 mm. This additional distance between MAST and the spacecraft enables significantly less strict magnetic
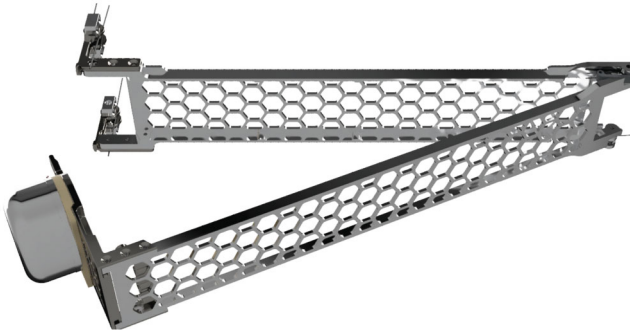
Fig. 8 FS2 twofold boom with fluxgate magnetometer on its tip. It achieves a separation to the spacecraft of over 620 mm. The undeployed boom extrudes only 9 mm from the surface of the satellite and is 6.4 cm wide

cleanliness requirements for the spacecraft and its subsystems, as magnetic flux diminishes quickly with increasing distance ($B \propto 1/r^3$).

The boom is currently under development by the Aalto University team and will be also built and tested with the in-house facilities.

A strict magnetic cleanliness program for the system and subsystem design is still needed to fulfil these requirements. Firstly, all magnetic disturbance sources surpassing magnetic emission limits onboard the spacecraft should be mitigated. Secondly, the remaining magnetic field sources should be characterised by determining their static and dynamic magnetic dipole moments.

Mitigation can be achieved primarily by avoiding the use of any magnetic materials and minimising or compensating current loops. Magnetic shielding that relies on magnetically soft materials should be avoided, if possible, as it poses a high risk of remagnetisation during the mission. Degaussing should be performed in order to minimise the amount of remnant magnetisation of the system. Any significant remaining MDMs have to be compensated for where possible; mutual compensation is preferred, but permanent compensation magnets should be used where necessary.

Intermediate magnetic screenings during the development process ensure magnetic interference mitigation. The custom magnetic test bed of Aalto University can be utilised for these characterisations (Monguiló 2021; Riwanto 2021; Monguiló et al. 2022).

4.5 Communication

The highly elliptic orbit of the mission poses potential challenges related to communication system design. For one, the high apogee of over 42,000 km of the mission results in a large Free Space Path Loss (FSPL), which heavily impacts the achievable data rate and performance of the communication system in different parts of the orbit. Furthermore, the large operating distance also introduces latency into the Radio Frequency (RF) link which complicates half-duplex operation. To combat these issues, a variable data rate is proposed for the radio system design, which enables scientific and telemetry data downlink throughout the mission. In addition, full-duplex communication simplifies the commanding and operation of the satellite, since the latency of the radio link does not have to be taken into account.

The proposed system will operate with three different data rates, which are applied at different sections of the satellite orbit. The data rate speeds were chosen to be 40.0 kbit/s, 2.5 kbit/s, 0.1 kbit/s so that the data downlink requirements are satisfied without complicating

Table 2 Foresail-2 transmission link budgets for uplink and downlink in apogee and perigee

	300 km [Perigee]		8800 km		41,800 km [Apogee]	
	Up	Down	Up	Down	Up	Down
Freq.	**2.08 GHz**	**2.28 GHz**	**2.08 GHz**	**2.28 GHz**	**2.08 GHz**	**2.28 GHz**
TX Power	45 dBm	30 dBm	45 dBm	30 dBm	45 dBm	30 dBm
System Loss	2.5 dB	1.6 dB	2.5 dB	1.6 dB	2.5 dB	1.6 dB
Antenna Gain	30.0 dB	−2.0 dB	30.0 dB	−2.0 dB	30.0 dB	−2.0 dB
EIRP	72.5 dBm	26.4 dBm	72.5 dBm	26.4 dBm	72.5 dBm	26.4 dBm
FSPL	148 dB	149 dB	178 dB	179 dB	191 dB	192 dB
Propagation Losses	4.3 dB	4.3 dB	4.3 dB	4.3 dB	4.3 dB	4.3 dB
Data rate	**40.0 kbit/s**	**40.0 kbit/s**	**2.5 kbit/s**	**2.5 kbit/s**	**0.1 kbit/s**	**0.1 kbit/s**
Tot. Path Loss	152.7 dB	153.5 dB	182.0 dB	1182.8 dB	195.6 dB	196.4 dB
Final E_b/E_n	**23.7 dB**	**23.0 dB**	**6.4 dB**	**5.7 dB**	**6.9 dB**	**6.1 dB**

the mission design. The ranges to which the data rates are applied are 300 km to 2300 km, 2300 km to 8800 km and 8800 km to 41,800 km respectively.

Table 2 shows the link budget for the up and downlink in the extreme cases of perigee and apogee communication for GTO and for the centre altitude of 8800 km. The Transmit Power (TX Power) represents the communication system's output power, while system loss is the loss in the system between the communication system and the satellite antenna. It includes the antenna efficiency. The antenna gain refers to the gain of both transmitting and receiving antennas. The Effective Isotropic Radiated Power (EIRP) denotes the RF power radiated by the satellite antenna, and FSPL is the Free Space Path Loss. In addition, the propagation losses are also taken into consideration and they include losses from antenna pointing errors, atmospheric absorption and losses due to polarization mismatch. The effect of FSPL and propagation losses results in the total path loss of the radio link, which is also shown in Table 2. In all cases, a suitable data rate was chosen to achieve a positive link margin of over 5.5 dB.

Another important factor to take into consideration, is the operating frequency of the satellite, as this heavily impacts the design of the communication system. The commercial S-band frequency range was chosen, as this offered improved data rates compared to lower bands such as UHF and VHF, without significant increases in propagation losses from environmental effects. To maximise the performance of the communication system, Phase Shift Keying (PSK) was chosen as the modulation technique for downlink and uplink. This was done since binary PSK and quadrature PSK offer good noise and distortion performance.

The S-band communication subsystem is based on flight heritage from the UHF system of Foresail-1. Thus, the s-Band subsystem will also be developed in-house at Aalto University (Clayhills 2022). Full-duplex operation is achieved by two separate antennas and dedicated transceiver sides for both RX and TX. In addition, the system also will include RF filters implemented on microstrips directly on the PCB, which improve the isolation and noise figure of the TX and RX sides. The large operating distance and the ground segment implementation result in low signal levels received at the satellite and as a result high receiver sensitivity is required with a minimal noise figure in the RX chain to achieve a positive link margin. Microstrip filters were preferred for the design over other available solutions, such as Surface Acoustic Wave filters since the specific properties and frequency ranges of microstrip filters can be tuned to the application at hand.
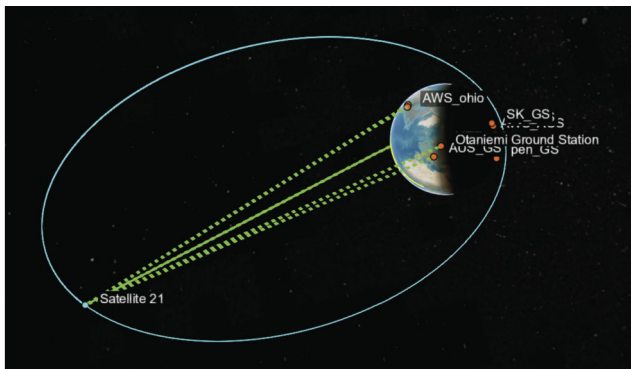
Fig. 9 Ground station network optimisation simulation for high elliptical 30° inclination orbit

The satellite mission data downlink budget requirements are satisfied with the designed omnidirectional dipole antennas. In addition to the in-house developed TX and RX dipole antennas, the system is intended to also utilise a higher gain patch antenna for communication at the apogee once attitude control of the spacecraft is achieved. The use of a directional antenna increases the link margin in the downlink link budget, which enables a higher achievable data rate for scientific and telemetry data transmission. In this scenario, the satellite uplink communication would still be performed via the RX dipole antenna, since satellite commanding must be possible at all times and there is a larger link margin in the uplink due to the transmission power of the ground station. At lower orbit altitudes, the satellite would switch back to utilise the TX and RX dipole antennas as the primary command link of the spacecraft. Together, this enables full-duplex communication at any point of the satellite orbit. A market analysis for the TX patch antenna is currently ongoing.

4.6 Ground Segment

The inclination of the orbit determines the link time for the satellite, while the altitude of the orbit affects the FSPL, causing more significant attenuation of radio signals.

As a result, the capabilities of the Aalto University ground station are insufficient to meet the data downlink demands of the mission. The combination of a 3 m S-Band dish antenna and the high latitude of the ground station (60°10′N) present challenges, resulting in large communication distances and limited link time.

To fulfil the mission data downlink requirements, the use of external Ground Station as a Service (GSaS) is being considered.

Even though the data rate in apogee is low, the mission data downlink requirements of 13 MB per day can be satisfied with this solution since the link time is large.

To determine the most suitable GSaS locations, a study is currently underway, utilising mission simulation software as shown in Fig. 9. The aim of this study is to provide insight into the best options for ensuring the successful completion of the satellite mission. In this scenario, the satellite commanding would be performed via the Aalto Ground Station, and the GSaS providers would be used solely for scientific and telemetry data downlink.

4.7 Electrical Power

Compared to LEO, solar cells undergo severe degradation in highly elliptical orbits. Simulations with MC-SCREAM (Messenger et al. 2008) in SPENVIS for a 6 month mission

Table 3 Power consumption of Foresail-2 subsystems for different operating modes. Total power consumption includes a 20% margin

Modes	Safe [W]	Commissioning [W]	Science [W]
OBDH	0.30	0.60	0.60
ADCS		9.3	3.3
EPS	0.72	1.0	1.0
COM	4.0	4.0	7.0
MAST		0.5	1.5
REPE		0.5	2.5
CDE		0.1	0.60
RadEx		0.1	0.30
Cameras		0.70	
Contingency	1.0	3.4	3.4
Total	**6.0**	**20**	**20**

Table 4 Power production reduction factors in Foresail-2

Angle reduction	6%
MPPT tracking accuracy	98%
Cell loss at maximum temperature	5%
Battery charging efficiency	90%
Radiation loss EOL	20%
Margin	20%
Total reduction	**50.4%**

lifetime show a degradation at the end of life (EOL) in the power generation at the maximum power point up to 30% with 100 μm thick cover glass and up to 20% with 150 μm thick cover glass. Cover glass thickness beyond 150 μm offers marginal improvements in degradation performance. The thermal environment is also challenging as the orbital period is longer compared to LEO. With the first attitude mode as seen in Fig. 7 the solar panels experience longer periods in the Sun, possibly decreasing power generation more compared to the LEO environment. Additionally, thermal studies showed that the average temperature of the solar panels might not rise higher than experienced in LEO.

The nominal power consumption of the mission is estimated to be around 20 W as seen in Table 3, with the communication subsystem requiring up to 7 W due to long communication distances. Combined with the power production reduction factors shown in Table 4, it is estimated that the required number of solar cells in the Sun is 42 when Azur Space 3G30A or similar are used. This amount of solar cells will yield excess production of 17.5 W h per orbit at EOL as shown in Table 5. The second discussed attitude mode would require significantly more solar cells as the irradiated solar panel area is constantly changing due to the alignment of the rotational axis. To simplify the EPS and attached system the first attitude mode is preferred.

With this mode, solar cells can be grouped into three 7s2p solar panels. One of the solar panels is body-mounted on the Y+ side, while the other two are deployable to the sides. There is a backup solar panel on the backside (Y-) of the satellite that provides power during initial tumbling and during operation of the CDE later in the mission, as the satellite begins to lose sun-pointing mode when the CDE tether is deployed. The solar panels will

Table 5 EOL energy balance of Foresail-2 in commissioning/science mode per orbit

Orbital period	690 min
Average time in the Sun	580 min
Average time in shadow	31 min
Power consumption	20 W
Power production	25.6 W
Total production	247.5 W h
Total consumption	230 W h
Excess production	**17.5 W h**
Battery capacity	40 W h
Total consumption in shadow	10.3 W h
DoD	**25.8%**

be designed and built in-house based on the design used for FS1 and FS1p (Palmroth et al. 2019).

The FS2 satellite will have a 2p2s 40 W h battery pack consisting of four COTS Panasonic NCR-18650B Li-ion cells. While the estimated depth-of-discharge is up to 26%, the battery will experience only up to 100 discharge-charge cycles. As NCA-type Li-ion cells can withstand up to 2000-3000 cycles, degradation of the capacity of Li-ion cells is not a problem. The battery pack is equipped with heaters based on previous simulations that showed that the overall temperature of the satellite is lower than in LEO (Naik 2019). In addition, the battery is equipped with a balancing circuit to maintain uniform charging of series cells.

The FS2 Electrical Power System (EPS) is an evolution of the EPS used in the FS1 mission and is developed in-house by the Aalto Platform team (Cheremetiev 2020). The EPS implements system simplicity and extensive testing, instead of redundancy, to tackle the challenging requirements. Implementing redundancy can be complex and time-consuming. Because the subsystem will be built predominantly with COTS components, environmental testing such as total dose and thermal tests are required to qualify the components. For mission-critical components, such as microcontrollers and memory chips, radiation-tolerant parts are selected. Possibly destructive single-event latch-ups are dealt through fault containment strategies, for example, by using latching current limiters to quickly power off functional blocks with latched components.

Reducing power generation stages through a combination of solar maximum peak power tracking and battery management makes the EPS not only simpler but also more efficient. Power distribution in FS2's EPS is also unusual as it provides only "raw" voltages to loads: regulated nominally 3.6 V and 6 V to 8.2 V battery voltage. The loads can generate their own supply voltages efficiently with required specifications that EPS otherwise would not be able to achieve.

4.8 On Board Data and Bus Architecture

The in-house developed OnBoard Data Handling (OBDH) of FS2 employs a simple bus architecture to manage all payloads and subsystems. To isolate the avionics from payload communications a central management system is connected to the avionics bus (AVI BUS) on one side and all the payloads on the other as seen in Fig. 10. The payloads CDE, REPE and MAST have a non-shared bus connection to reduce crosstalk. Engineering cameras
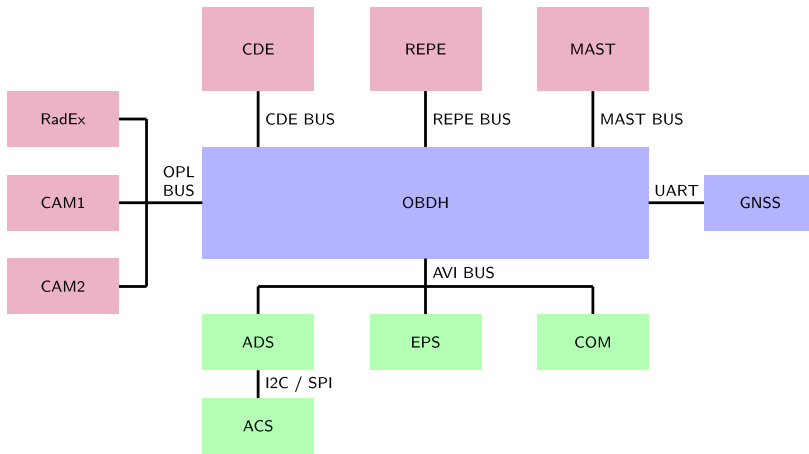
Fig. 10 Foresail-2 onboard data bus architecture with each bus redundant

(CAM1 and CAM2) and RadEx share one bus connection (OPL BUS) to the OBDH. All buses are redundant to ensure operational capabilities even if one bus gets into a deadlock situation. The GNSS subsystem is communicating non-redundantly with the OBDH.

An external memory bank is used onboard the OBDH subsystem to hold and buffer housekeeping and telemetry logs from the rest of the satellite prior to transferring them to storage. Data can then be transferred to the S-Band subsystem, which handles the encoding, antenna selection and linking.

Additionally, the deployment of the boom is initiated and observed by the OBDH. Also, the solar panel deployment is handled by this system as their entire area is not needed at the beginning of the mission.

The main processor will be a VA41620 – Radiation Hardened Arm® Cortex®-M4. Despite the radiation shielding the decision was made to use this microprocessor as it reduces the risks for severe single-event radiation effects. Smaller key components like bus transceivers are planned to undergo a radiation screening process to find the most suitable one.

4.9 Structure

Based on the analysis, a 6U form factor ($100.0 \times 226.3 \times 340.5$ mm^3) is feasible as shown in Fig. 11. As the smaller specification with only 340.5 mm rail length is compatible with more satellite dispensers, the satellite design differs from the 6U CubeSat standard which only specifies the longer XL version with 366.0 mm (Poly 2022).

With the attitude mode 1 as shown in Fig. 7 the following structure and payload placements with respect to the spacecraft body axis in a 6U form factor can be proposed.

As seen in Fig. 12 the tether deployment and the REPE field of view are in the Z+ axis direction. Two solar panels that are folded up on the Y+ panel will be deployed early on in the mission. The position of solar panels after deployment will be parallel with the Y+ solar panel.

Two dipole antennas will deploy on the Z+ panel. The patch antenna is located on the Y-face so that its lobe is directed towards Earth once the spacecraft spins around the Y axis pointing towards the sun.
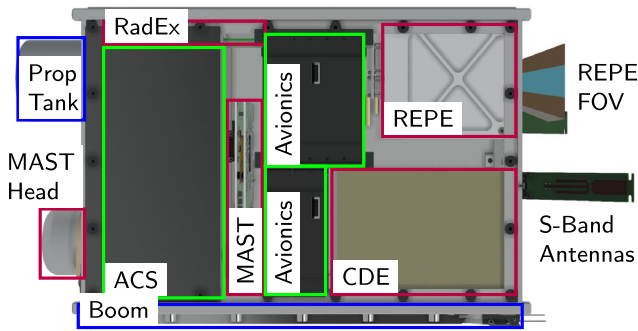
Fig. 11 Preliminary subsystem layout of the Foresail-2 satellite within the 6U chassis $(100.0 \times 226.3 \times 340.5 \text{ mm}^3)$
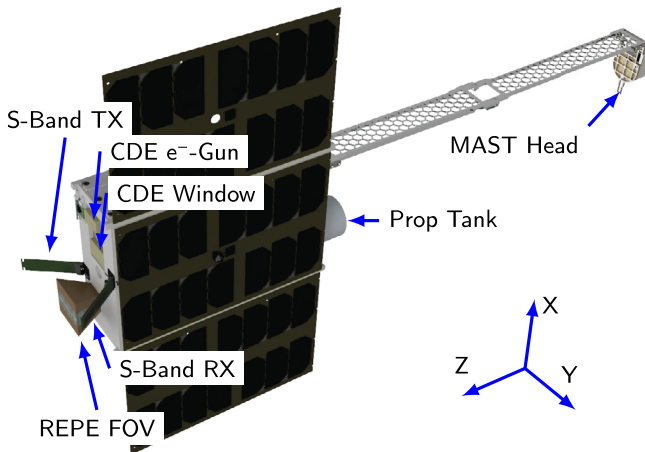
Fig. 12 Foresail-2 satellite in science configuration (deployed solar panels, antennas and boom) with important aspects marked out

The fluxgate magnetometer head is mounted to the end of the boom, which is located within the Tuna Can volume of the launch pod in the undeployed state. The undeployed boom is located on the X+ side and the opening is realised with a two stage deployment. The magnetometer boom is deployed in the Z-axis direction in the spacecraft body frame. The second Tuna Can volume can be used as a propellant tank for the ACS. The boom will protrude more from the surface of the satellite as the allowed 6.5 mm by the CubeSat standard (Poly 2022). A market analysis has shown that most of the satellite dispensers can allow up to 10 mm of protrusion, which has been set as a requirement for the FS2 spacecraft (Tolstoj and Rose 2022).

With this configuration the satellite mass is around 15 kg as seen in Table 6. The fuel mass has been already included in the ADCS budget. The CubeSat is not compliant with the 12 kg maximum as stated in the standard (Poly 2022), but modern CubeSat dispensers are capable of up to 16 kg for one 6U slot (e.g. (Tolstoj and Rose 2022)).

Table 6 Mass Budget for the Foresail-2 spacecraft. Margins of the subsystems vary due to different heritage and TRL levels. ADCS subsystem includes fuel

Subsystem	Planned [g]	Contingency [g]	Total [g]
OBDH	223	32	255
EPS	400	70	470
ADCS	1130	226	1356
COM	380	76	456
Structure	5466	673	6139
Payloads	2820	524	3344
Wires		5%	601
Margin		20%	2404
Total			**15,025**

5 Discussion

As stated in S1.3 the measured science data of the FS2 mission has to be compared and combined with other mission data. FS2 will explore the high-radiation environment of the Van-Allen belts, where no CubeSat has been operated to this date. The following short overview of selected other missions will provide a better understanding of the possible collaboration candidates, that are under development.

GTOSat is a 6U CubeSat with similar aims in terms of orbit and science to FS2 (Lucas et al. 2022). It is fully built and tested and is waiting for a launch opportunity. It carries a Relativistic Electron Magnetic Spectrometer (REMS) and a fluxgate MAGnetometer (MAG). REMS measures electrons in the energy range of 0.2 MeV to 1 MeV and protons from 0.2 MeV to 8 MeV. MAG is placed at the end of a four-segment one-metre boom measuring $\pm$ 4096 nT at 0.125 nT resolution and $\pm$ 65,536 nT at 2.0 nT resolution. The sensor Root Mean Square (RMS) noise level is < 0.1 nT and the sensitivity threshold is 0.01 nT Hz^{-2}. The planned nominal orbital altitude is between 185 km and 35,000 km with the inclination of $< 25°$. An S-Band transceiver with two patch antennas is used to transmit data at >1 Mbit/s near the perigee through NASA's Near Earth Network of ground stations. Mitigation of radiation effects is accomplished through a multi-pronged systems approach including parts selection and shielding. This should reduce the total dose for 1 year on orbit to less than 30 krad (Blum et al. 2020; Barney et al. 2022).

M-BARC is being developed to carry four magnetometers to measure with the resolution of 1.65 nT at 1 Hz. The launch was scheduled for 2019, but not confirmed. Currently, no further information on the project has been found. The instrument is designed to detect the ULF waves in the PC1 to PC5 range. The M-BARC team plans a 3-month mission in GTO (Regoli et al. 2018).

SpectroCube is a spectroscopy platform being developed for astrobiology and astrochemistry experiments carrying sample compartments and a spectrometer. Currently the launch date is unknown. The satellite is designed to be launched into a Highly Elliptical Orbit (HEO) around Earth. GTO is selected as the baseline orbit with super-GTO being a viable option. The total mission lifetime is expected to last around 200 days. The satellite carries four reaction wheels, three magnetorquers, sun sensors, cold gas propulsion, an S-band transceiver and patch antennas. Shielding of the main electronic components is used to reduce locally the total ionising radiation dose below 20 krad (Elsaesser et al. 2020).

The scientific objectives and instrument set of GTOSat and M-BARC are similar to FS2, providing an opportunity to compare measurements, results and in-orbit experience. Spec-

troCube's orbit, lifetime and therefore radiation shielding requirements can help during the design process.

GTOSat, SpectroCube and M-BARC missions show that high altitude and high eccentricity orbits are desirable but challenging. The unique radiation environment is a subject of scientific study by itself and could provide high-radiation exposure for several different experiments.

6 Conclusion

As Earth's radiation belts are extremely important for space weather and the Van Allen Probes have ceased operation since 2019, the FORESAIL consortium wants to measure high-energy particle fluxes to better understand the dynamics of the radiation belts during a period of intense magnetic activity. Therefore, this mission analysis study was conducted and concluded with the design of the Foresail-2 satellite. The primary science goals are to measure magnetic ULF waves and the plasma environment in the magnetosphere around Earth. The proposed science for the Foresail-2 mission sets unique requirements that come from its orbit and instruments. Three payloads, MAST, REPE and CDE, are dedicated to ULF wave measurements and to the understanding of the plasma environment around Earth. Additionally, CDE will demonstrate E-sailing capabilities and a novel deorbiting technique. A fourth payload investigates multilayer radiation shielding to minimise TID.

In this study, it was shown that the mission can be achieved with a 6U CubeSat platform using mostly COTS components. The lifetime for this spacecraft class in highly elliptical orbit is limited because of the environmental effects. With the presented shielding solution the radiation level inside the satellite is expected to remain under 12 krad for the mission duration of one year. Due to a high dependence between the orbit insertion and the orbital lifetime, a separate deorbiting solution is needed. This will ensure that space sustainability regarding space debris can be achieved. The deorbiting solution also opens up a wider range of launch opportunities, a crucial advantage given the limited ride-share offerings to highly elliptical orbits.

With the design presented in this paper, FS2 is well-suited for the demanding environment of a highly elliptical orbit and thus capable of meeting its scientific objectives.

Declarations

References

Agostinelli S, Allison J, Amako K, Apostolakis J, Araujo H, Arce P et al (2003) Geant4–a simulation toolkit. Nucl Instrum Methods Phys Res A 506(3):250–303. https://doi.org/10.1016/S0168-9002(03)01368-8

Allen JAV, Ludwig GH, Ray EC, McIlwain CE (1958) Observation of high intensity radiation by satellites 1958 alpha and gamma. J Jet Propuls 28:588–592

Allison J, Amako K, Apostolakis J, Araujo H, Arce Dubois P, Asai M et al (2006) Geant4 developments and applications. IEEE Trans Nucl Sci 53(1):270–278

Allison J, Amako K, Apostolakis J, Arce P, Asai M, Aso T et al (2016) Recent developments in Geant4. Nucl Instrum Methods Phys Res A 835:186–225.

Anderson BJ, Engebretson MJ, Rounds SP, Zanetti LJ, Potemra TA (1990) A statistical study of Pc 3-5 pulsations observed by the AmMPTE/CCE magnetic fields experiment 1. Occurrence distributions. J Geophys Res 95(A7):495–10523

Anger M (2023) Foresail-2 orbital lifetime analysis. https://doi.org/10.5281/zenodo.7646875

Auer M, Scherzer M, Valavanoglou A, Leitner S, Magnes W (2018) Front-end asic for spaceborne fluxgate-magnetometers. In: Microelectronics systems symposium (MESS). http://www.mess.co.at

Baker DN, Kanekal SG, Hoxie VC, Henderson MG, Li X, Spence HE, Elkington SR, Friedel RHW, Goldstein J, Hudson MK, Reeves GD, Thorne RM, Kletzing CA, Claudepierre SG (2013) A long-lived relativistic electron storage ring embedded in Earth's outer Van Allen belt. Science 340(6129):186–190

Baker DN, Erickson PJ, Fennell JF, Foster JC, Jaynes AN, Verronen PT (2018) Space weather effects in the Earth's radiation belts. Space Sci Rev 214(1):1–60. https://doi.org/10.1007/s11214-017-0452-7

Baker DN, Hoxie V, Zhao H, Jaynes AN, Kanekal S, Li X, Elkington S (2019) Multiyear measurements of radiation belt electrons: acceleration, transport, and loss. J Geophys Res Space Phys 124(4):2588–2602

Barney J, Garduno O, Roecker C, Kroupa M, Holloway M, Schirato R, Maldonado CA, Arnold D, Larsen BA, Miller Z, Smith K, Wakeford D (2022) Experiment for space radiation analysis, energetic charged particle sensor: a charged particle telescope with novel sensors for measuring Earth's radiation belts. In: 2022 IEEE aerospace conference (AERO), pp 1–7. https://doi.org/10.1109/AERO53065.2022.9843784

Bentley SN, Watt CEJ, Owens MJ, Rae IJ (2018) ULF wave activity in the magnetosphere: resolving solar wind interdependencies to identify driving mechanisms. J Geophys Res Space Phys 123(4):2745–2771

Blake JB, Kolasinski WA, Fillius RW, Mullen EG (1992) Injection of electrons and protons with energies of tens of MeV into L < 3 on 24 March 1991. Geophys Res Lett 19(8):821–824

Blum LW, Bonnell JW, Agapitov O, Paulson K, Kletzing C (2017) EMIC wave scale size in the inner magnetosphere: observations from the dual Van Allen probes. Geophys Res Lett 44(3):1227–1233

Blum L, Kepko L, Turner D, Gabrielse C, Jaynes A, Kanekal S, Schiller Q, Espley J, Sheppard D, Santos L, Lucas J, West S (2020) The GTOSat CubeSat: scientific objectives and instrumentation. In: Islam MS, George T (eds) Micro- and nanotechnology sensors, systems, and applications XII, p 10

Bonhomme GL (2020) Foresail-2 aocs trade studies and design. Master's thesis, Aalto University. http://urn.kb.se/resolve?urn=urn:nbn:se:ltu:diva-80707

Brito TV, Halford AJ, Elkington SR (2020) Ultralow frequency-wave induced losses. In: Jaynes AN, Usanova ME (eds) The dynamic loss of Earth's radiation belts. Elsevier, Amsterdam, pp 29–48. https://doi.org/10.1016/B978-0-12-813371-2.00002-0

Cal Poly (2022) CubeSat design specification rev. 14.1. https://www.cubesat.org/cubesatinfo

Chen H, Gao X, Lu Q, Wang S (2019) Analyzing EMIC waves in the inner magnetosphere using long-term Van Allen probes observations. J Geophys Res Space Phys 124(9):7402–7412

Cheremetiev K (2020) Design of reliable electrical power system for foresail-1 small satellite. Master's thesis, Aalto University. https://aaltodoc.aalto.fi:443/handle/123456789/44369

Claudepierre SG, Mann IR, Takahashi K, Fennell JF, Hudson MK, Blake JB, Roeder JL, Clemmons JH, Spence HE, Reeves GD, Baker DN, Funsten HO, Friedel RHW, Henderson MG, Kletzing CA, Kurth WS, MacDowall RJ, Smith CW, Wygant JR (2013) Van Allen probes observation of localized drift resonance between poloidal mode ultra-low frequency waves and 60 keV electrons. Geophys Res Lett 40(17):4491–4497

Clausen LBN, Baker JBH, Ruohoniemi JM, Singer HJ (2011) EMIC waves observed at geosynchronous orbit during solar minimum: statistics and excitation. J Geophys Res Space Phys 116(A10):A10205

Clayhills B (2022) Design of a transceiver front-end for the foresail-2 small satellite. Master's thesis, Aalto University. https://aaltodoc.aalto.fi/handle/123456789/118338

CubeSpace (2023) Cubewheel gen 2 product description. https://www.cubespace.co.za/products/gen-2/actuators/cubewheel/

Denton RE, Ofman L, Shprits YY, Bortnik J, Millan RM, Rodger CJ, da Silva CL, Rogers BN, Hudson MK, Liu K, Min K, Glocer A, Komar C (2019) Pitch angle scattering of sub-MeV relativistic electrons by electromagnetic ion cyclotron waves. J Geophys Res Space Phys 124(7):5610–5626

Donder ED, Messios N, Calders S, Calegaro A, Mezhoud S (2018) Space environment information system: Spenvis. 04.05.2018. https://www.spenvis.oma.be/

Elkington SR (2006) A review of ulf interactions with radiation belt electrons. In: Takahashi K, Chi PJ, Denton RE, Lysak RL (eds) Magnetospheric ULF waves: synthesis and new directions. American Geophysical, Union, pp 177–193

Elkington SR, Hudson MK, Chan AA (2003) Resonant acceleration and diffusion of outer zone electrons in an asymmetric geomagnetic field. J Geophys Res Space Phys 108(A3):1116

Elsaesser A, Merenda F, Lindner R, Walker R, Buehler S, Boer G, Villa A, Hallak Y, Aguado F, Alberti E, Wood B (2020) Spectrocube: a European 6U nanosatellite spectroscopy platform for astrobiology and astrochemistry. Acta Astronaut 170:275–288

Fetzer A (2023a) Simulated shielding performance of 1728 three-layer permutations of 12 common satellite and radiation shielding materials against trapped particles on GTO. https://doi.org/10.5281/zenodo.7620703

Fetzer A (2023b) Simulated shielding performance of 1296 four-layer permutations of six common satellite and radiation shielding materials against trapped particles on gto. https://doi.org/10.5281/zenodo.7621281

Fetzer A (2023c) Simulated shielding performance of 1024 five-layer permutations of four satellite and radiation shielding materials against trapped particles on gto. https://doi.org/10.5281/zenodo.7622159

Fetzer A (2023d) Shielding performance of the 98 first chemical elements against trapped particles on gto. https://doi.org/10.5281/zenodo.7616012

Fetzer A (2023e) Simulated shielding performance of 2500 two-layer permutations of the first 50 chemical elements against trapped particles on GTO. https://doi.org/10.5281/zenodo.7828929

Fetzer A, Anger M, Kärkkäinen T, Olivella AE, Praks J (2023a) Radiation shielding experiment for cubesat on highly elliptical orbit. In: Abstract and presentation at the Space Environment Monitoring Workshop (SPACEMON), Conference date: 15-05-2023 Through 17-05-2023. https://research.aalto.fi/en/publications/radiation-shielding-experiment-for-cubesat-on-highly-elliptical-o

Fetzer A, Anger M, Oleynik P, Praks J (2023b) Total ionising dose multilayer shielding optimisation for nanosatellites on geostationary transfer orbit. Submitted to Adv Space Res. 16 Jun 2023

Fraser BJ, Loto'Aniu TM, Singer HJ (2006) Electromagnetic ion cyclotron waves in the magnetosphere. In: Magnetospheric ULF waves: synthesis and new directions, vol 169, p 195

Gieseler J, Oleynik P, Hietala H, Vainio R, Hedman H-P, Peltonen J, Punkkinen A, Punkkinen R, Säntti T, Hæggström E, Praks J, Niemelä P, Riwanto B, Jovanovic N, Mughal MR (2020) Radiation monitor RADMON aboard Aalto-1 CubeSat: first results. Adv Space Res 66(1):52–65. https://doi.org/10.1016/j.asr.2019.11.023

Gieseler J, Janhunen P, Kilpua E, Vainio R, Palmroth M, Oleynik P, Hedman H-P, Punkkinen A, Punkkinen R, Salomaa L, Säntti T, Tuominen J, Virtanen P, Praks J, Slavinskis A, Rameez Kakakhel S, Plosila J, Tammi J, Tenhunen H, Westerlund T (2021) Particle telescope PATE onboard FORESAIL-1 CubeSat. In: 43rd COSPAR scientific assembly. Held 28 January - 4 February, vol 43, p 1152

Glaßmeier K-H (2007) Geomagnetic pulsations. In: Gubbins D, Herrero-Bervera E (eds) Encyclopedia of geomagnetism and paleomagnetism. Springer, Berlin, pp 333–334

GOMSpace (2020) Nanoprop 6DOF module-key features. https://gomspace.com/UserFiles/Subsystems/flyer/Flyer_NanoProp_6DOF.pdf

Hartinger MD, Reeves GD, Boyd A, Henderson MG, Turner DL, Komar CM, Claudepierre SG, Mann IR, Breneman A, Di Matteo S, Zhang X-J (2020) Why are there so few reports of high-energy electron drift resonances? Role of radial phase space density gradients. J Geophys Res Space Phys 125(8):e2020JA027924. https://doi.org/10.1029/2020JA027924

He F, Guo R-L, Dunn WR, Yao Z-H, Zhang H-S, Hao Y-X, Shi Q-Q, Rong Z-J, Liu J, Tian A-M, Zhang X-X, Wei Y, Zhang Y-L, Zong Q-G, Pu Z-Y, Wan W-X (2020) Plasmapause surface wave oscillates the magnetosphere and diffuse aurora. Nat Commun 11:1668

Iakubivskyi I, Janhunen P, Praks J, Allik V, Bussov K, Clayhills B, Dalbins J, Eenmäe T, Ehrpais H, Envall J, Haslam S, Ilbis E, Jovanovic N, Kilpua E, Kivastik J, Laks J, Laufer P, Merisalu M, Meskanen M, Märk R, Nath A, Niemelä P, Noorma M, Mughal MR, Nyman S, Pajusalu M, Palmroth M, Paul AS, Peltola T, Plans M, Polkko J, Islam QS, Reinart A, Riwanto B, Sammelselg V, Sate J, Sünter I, Tajmar M, Tanskanen E, Teras H, Toivanen P, Vainio R, Väänänen M, Slavinskis A (2020) Coulomb drag propulsion experiments of ESTCube-2 and Foresail-1. Acta Astronaut 177:771-783

Janhunen P (2004) Electric Sail for Spacecraft Propulsion J Propuls Power 20. https://doi.org/10.2514/1.8580

Janhunen P, Sandroos A (2007) Simulation study of solar wind push on a charged wire: basis of solar wind electric sail propulsion. Ann Geophys 25:755–767. https://doi.org/10.5194/angeo-25-755-2007

Janhunen P, Quarta AA, Mengali G (2013) Electric solar wind sail mass budget model. Geosci Instrum Method Data Syst 2:85–95. https://doi.org/10.5194/gi-2-85-2013

Jaynes AN, Ali AF, Elkington SR, Malaspina DM, Baker DN, Li X, Kanekal SG, Henderson MG, Kletzing CA, Wygant JR (2018) Fast diffusion of ultrarelativistic electrons in the outer radiation belt: 17 March 2015 storm event. Geophys Res Lett 45(20):10874–10882

Jun C-W, Miyoshi Y, Kurita S, Yue C, Bortnik J, Lyons L, Nakamura S, Shoji M, Imajo S, Kletzing C, Kasahara Y, Kasaba Y, Matsuda S, Tsuchiya F, Kumamoto A, Matsuoka A, Shinohara I (2021) The characteristics of EMIC waves in the magnetosphere based on the Van Allen probes and Arase observations. J Geophys Res Space Phys 126(6):e29001

Kalliokoski MM, Kilpua EK, Osmane A, Turner D, Jaynes A, Turc L, George H, Palmroth M (2020) Outer radiation belt and inner magnetospheric response to sheath regions of coronal mass ejections: a statistical analysis. Ann Geophys 38(3):683–701

Kokubun S, Kivelson MG, McPherron RL, Russell CT, West HI Jr (1977) Ogo 5 observations of Pc 5 waves: particle flux modulations. J Geophys Res (1896-1977) 82(19):2774–2786. https://doi.org/10.1029/JA082i019p02774

Koons HC, Fennell JF (2006) Space weather effects on communications satellites. URSI Radio Sci Bull 2006(316):27–41

Kopacz JR, Herschitz R, Roney J (2020) Small satellites an overview and assessment. Acta Astronaut 170:93–105. https://doi.org/10.1016/j.actaastro.2020.01.034

Lamy A, Fevre CL, Sarli B (2012) Analysis of geostationary transfer orbit long term evolution and lifetime. J Aerosp Eng Sci Appl 4:12–27

Leijtens J (2021) MAUS sun sensor product specification document. https://lens-rnd.com/products/maus-drw-nr:-114t000

Lejosne S, Kollmann P (2020) Radiation belt radial diffusion at Earth and beyond. Space Sci Rev 216(1):19

Lejosne S, Allison HJ, Blum LW, Drozdov AY, Hartinger MD, Hudson MK, Jaynes AN, Ozeke L, Roussos E, Zhao H (2022) Differentiating between the leading processes for electron radiation belt acceleration. Front Astron Space Sci 9:896245

Liu W, Sarris TE, Li X, Elkington SR, Ergun R, Angelopoulos V, Bonnell J, Glassmeier KH (2009) Electric and magnetic field observations of Pc4 and Pc5 pulsations in the inner magnetosphere: a statistical study. J Geophys Res Space Phys 114(A12):A12206

Liu W, Sarris TE, Li X, Ergun R, Angelopoulos V, Bonnell J, Glassmeier KH (2010) Solar wind influence on Pc4 and Pc5 ULF wave activity in the inner magnetosphere. J Geophys Res Space Phys 115(A12):A12201

Liu W, Sarris TE, Li X, Zong QG, Ergun R, Angelopoulos V, Glassmeier KH (2011) Spatial structure and temporal evolution of a dayside poloidal ulf wave event. Geophys Res Lett 38(19):L19104

Lucas J, Grubb M, Morris J, Suder M, Zemerick S, Blum L, Kepko L, Azimi B, Claggett C, Cudmore A, Espley J, Fraction J, Gruesbeck J, Khalifi H, Madden M, Murphy S, Odom J, Roder R, Rusley D, Santos L, Sheppard D, Shumko M, Starin S, Tsui E, West S, Valliant J, Gabrielse C, Crain S, Crain W, Chavez W, Maul G, Galchenko P, Daisey T, Green T, Hammer I, Hesh S, Thomson L, Alexa J, Sankaran S, Turner D (2022) Gtosat: radiation belt dynamics from the inside. In: Small satellite conference. https://digitalcommons.usu.edu/smallsat/2022/all2022/145/

Madry S, Pelton JN (2020) Historical perspectives on the evolution of small satellites. In: Pelton JN, Madry S (eds) Handbook of Small Satellites. Springer, Cham, pp 33–48. https://doi.org/10.1007/978-3-030-36308-6_2

Mathie RA, Mann IR (2001) On the solar wind control of pc5 ulf pulsation power at mid-latitudes: implications for MeV electron acceleration in the outer radiation belt. J Geophys Res Space Phys 106(A12):783–29796. https://doi.org/10.1029/2001JA000002

McPherron RL (2005) Magnetic pulsations: their sources and relation to solar wind and geomagnetic activity. Surv Geophys 26(5):545–592

Menk FW (2011) Magnetospheric ULF waves: a review. In: Liu W, Fujimoto M (eds) The dynamic magnetosphere, vol 3, pp 223–256

Messenger SR, Walters RJ, Warner JH, Evans H, Taylor SJ, Baur C, Heynderickx D (2008) Status of implementation of displacement damage dose method for space solar cell degradation analyses. In: Lacoste H, Ouwehand L (eds) 8th European space power conference. ESA special publication, vol 661, p 98

Min K, Lee J, Keika K, Li W (2012) Global distribution of EMIC waves derived from THEMIS observations. J Geophys Res Space Phys 117(5):A05219

Monguiló AS (2021) Magnetic moment characterization for small satellites. Master's thesis, Aalto University. https://aaltodoc.aalto.fi/handle/123456789/110575

Monguiló AS, Riwanto BA, Praks J (2022) Assessment of a machine-vision-assisted test bed for spacecraft magnetic cleanliness analysis. In: 4th symposium on space educational activities Barcelona. https://upcommons.upc.edu/handle/2117/370775

Mughal MR, Praks J, Vainio R, Janhunen P, Envall J, Näsilä A, Oleynik P, Niemelä P, Nyman S, Slavinskis A, Gieseler J, Jovanovic N, Riwanto B, Toivanen P, Leppinen H, Tikka T, Punkkinen A, Punkkinen

R, Hedman HP, Lill JO, Slotte JM (2021) Aalto-1, multi-payload cubesat: in-orbit results and lessons learned. Acta Astronaut 187:557–568

Murphy KR, Inglis AR, Sibeck DG, Watt CEJ, Rae IJ (2020) Inner magnetospheric ULF waves: the occurrence and distribution of broadband and discrete wave activity. J Geophys Res Space Phys 125(9):e27887

Naik KP (2019) A thermal investigation and comparative study of the foresail missions. Master's thesis, Luleå University of Technology. http://www.diva-portal.org/smash/get/diva2:1348295/FULLTEXT01.pdf

Nasa (1996) Space radiation effects on electronic components in low-Earth orbit: Practice no. pd-ed-1258. https://extapps.ksc.nasa.gov/Reliability/Documents/Preferred_Practices/1258.pdf

Nikitina L, Trichtchenko L (2021) Dynamics of electron flux in the slot region and geomagnetic activity. Space Weather 19(4):e2020SW002661

Oleynik P, Punkkinen A, Punkkinen R, Säntti T, Virtanen P, Salomaa L, Lethi J, Raukunen O, Tiensuu K, Praks J, Vainio R (2023) Cubesat particle instruments at the university of Turku. SPACEMON: Space Environment Monitoring Workshop

Osmane A, Kilpua E, George H, Allanson O, Kalliokoski M (2023) Linear, quasi-linear and nonlinear radial transport in the Earth's radiation belts. arXiv e-prints arXiv:2304.03009

Palmroth M, Praks J, Vainio R, Janhunen P, Kilpua EK, Afanasiev A, Ala-Lahti M, Alho A, Asikainen T, Asvestari E, Battarbee M, Binios A, Bosser A, Brito T, Dubart M, Envall J, Ganse U, Ganushkina NY, George H, Gieseler J, Good S, Grandin M, Haslam S, Hedman HP, Hietala H, Jovanovic N, Kakakhel S, Kalliokoski M, Kettunen VV, Koskela T, Lumme E, Meskanen M, Morosan D, Mughal MR, Niemelä P, Nyman S, Oleynik P, Osmane A, Palmerio E, Peltonen J, Pfau-Kempf Y, Plosila J, Polkko J, Poluianov S, Pomoell J, Price D, Punkkinen A, Punkkinen R, Riwanto B, Salomaa L, Slavinskis A, Säntti T, Tammi J, Tenhunen H, Toivanen P, Tuominen J, Turc L, Valtonen E, Virtanen P, Westerlund T (2019) Foresail-1 cubesat mission to measure radiation belt losses and demonstrate deorbiting. J Geophys Res Space Phys 124:5783–5799. https://doi.org/10.1029/2018JA026354

Pons AP, Noomen R (2019) Ariane 5 GTO debris mitigation using natural perturbations. Adv Space Res 63:1992–2002

Praks J, Mughal MR, Vainio R, Janhunen P, Envall J, Oleynik P, Näsilä A, Leppinen H, Niemelä P, Slavinskis A, Gieseler J, Toivanen P, Tikka T, Peltola T, Bosser A, Schwarzkopf G, Jovanovic N, Riwanto B, Kestilä A, Punkkinen A, Punkkinen R, Hedman HP, Säntti T, Lill JO, Slotte JM, Kettunen H, Virtanen A (2021) Aalto-1, multi-payload cubesat: design, integration and launch. Acta Astronaut 187:370–383

Regoli L, Moldwin M, Thoma J, Pellioni M, Bronner B (2018) Four-magnetometer board for cubesat applications. In: Small satellite conference

Ripoll JF, Claudepierre SG, Ukhorskiy AY, Colpitts C, Li X, Fennell JF, Crabtree C (2020) Particle dynamics in the Earth's radiation belts: review of current research and open questions. J Geophys Res Space Phys 125(5):e2019JA026735. https://doi.org/10.1029/2019JA026735

Riwanto BA (2021) Calibration and testing techniques for nanosatellite attitude system development in magnetic environment. Ph.D. dissertation, Aalto University. https://aaltodoc.aalto.fi/handle/123456789/109062

Russell C (2000) The solar wind interaction with the Earth's magnetosphere: a tutorial. IEEE Trans Plasma Sci 28(6):1818–1830

Saikin AA, Zhang JC, Allen RC, Smith CW, Kistler LM, Spence HE, Torbert RB, Kletzing CA, Jordanova VK (2015) The occurrence and wave properties of H^+-, He^+-, and O^+-band EMIC waves observed by the Van Allen probes. J Geophys Res Space Phys 120(9):7477–7492

Saikin AA, Zhang JC, Smith CW, Spence HE, Torbert RB, Kletzing CA (2016) The dependence on geomagnetic conditions and solar wind dynamic pressure of the spatial distributions of EMIC waves observed by the Van Allen probes. J Geophys Res Space Phys 121(5):4362–4377

Sandhu JK, Rae IJ, Wygant JR, Breneman AW, Tian S, Watt CEJ, Horne RB, Ozeke LG, Georgiou M, Walach MT (2021) ULF wave driven radial diffusion during geomagnetic storms: a statistical analysis of Van Allen probes observations. J Geophys Res Space Phys 126(4):e29024

Sarris TE, Li X, Zhao H, Papadakis K, Liu W, Tu W, Angelopoulos V, Glassmeier K-H, Miyoshi Y, Matsuoka A, Shinohara I, Imajo S (2022) Distribution of ULF wave power in magnetic latitude and local time using THEMIS and Arase measurements. J Geophys Res Space Phys 127(10):e2022JA030469

Shields J, Pong C, Lo K, Jones L, Mohan S, Marom C, Mckinley I, Wilson W, Andrade L (2017) Characterization of cubesat reaction wheel assemblies. J Small Satell 6:565. https://jossonline.com/page_id2037

Sigsbee K, Kletzing CA, Faden J, Smith CW (2023) Occurrence rates of electromagnetic ion cyclotron (EMIC) waves with rising tones in the Van Allen probes data set. J Geophys Res Space Phys 128(2):e2022JA030548. https://doi.org/10.1029/2022JA030548

Sinclair D, Dyer J (2013) Radiation effects and cots parts in smallsats. In: 27 th annual AIAA/USU conference on small satellites. https://digitalcommons.usu.edu/smallsat/2013/all2013/69/

Summers D, Thorne RM (2003) Relativistic electron pitch-angle scattering by electromagnetic ion cyclotron waves during geomagnetic storms. J Geophys Res Space Phys 108(A4):1143. https://doi.org/10.1029/2002JA009489

Tajmar M (2012) Survey on FEEP neutraliser options. https://doi.org/10.2514/6.2002-4243

Takahashi K, Bonnell J, Glassmeier K-H, Angelopoulos V, Singer HJ, Chi PJ, Denton RE, Nishimura Y, Lee D-H, Nosé M, Liu W (2010) Multipoint observation of fast mode waves trapped in the dayside plasmasphere. J Geophys Res Space Phys 115(A12):A12247

Takahashi K, Yumoto K, Claudepierre SG, Sanchez ER, Troshichev OA, Janzhura AS (2012) Dependence of the amplitude of Pc5-band magnetic field variations on the solar wind and solar activity. J Geophys Res Space Phys 117(A4):A04207

Thorne RM (2010) Radiation belt dynamics: the importance of wave-particle interactions. Geophys Res Lett 37(22):22107. https://doi.org/10.1029/2010GL044990

Tolstoj M, Rose J (2022) Exopod nova user manual rev. 1. https://exolaunch.com/documents/EXOpod_Nova_User_Manual_September_2022.pdf

Torbert RB, Russell CT, Magnes W, Ergun RE, Lindqvist PA, LeContel O, Vaith H, Macri J, Myers S, Rau D, Needell J, King B, Granoff M, Chutter M, Dors I, Olsson G, Khotyaintsev YV, Eriksson A, Kletzing CA, Bounds S, Anderson B, Baumjohann W, Steller M, Bromund K, Le G, Nakamura R, Strangeway RJ, Leinweber HK, Tucker S, Westfall J, Fischer D, Plaschke F, Porter J, Lappalainen K (2016) The fields instrument suite on MMS: scientific objectives, measurements, and data products. Space Sci Rev 199:105–135. https://doi.org/10.1007/s11214-014-0109-8

Turner DL, Shprits Y, Hartinger M, Angelopoulos V (2012) Explaining sudden losses of outer radiation belt electrons during geomagnetic storms. Nat Phys 8(3):208–212

Usanova ME, Mann IR, Darrouzet F (2016) EMIC waves in the inner magnetosphere. In: Low-frequency waves in space plasmas. Geophysical monograph series, vol 216. American Geophysical Union, Washington, pp 65–78

Vainio R, Desorgher L, Heynderickx D, Storini M, Flückiger E, Horne RB et al (2009) Dynamics of the Earth's particle radiation environment. Space Sci Rev 147(3–4):187–231

Van Allen JA, Frank LA (1959) Radiation around the Earth to a radial distance of 107,400 km. Nature 183:430–434

Wang Y, Luo X, Wu X (2020) Long-term evolution and lifetime analysis of geostationary transfer orbits with solar radiation pressure. Acta Astronaut 175:405–420

Winokur PS, Lum GK, Shaneyfelt MR, Sexton FW, Hash GL, Scott L (1999) Use of cots microelectronics in radiation environments. IEEE Trans Nucl Sci 46(6Pt1):12. https://www.osti.gov/biblio/20014703

Authors and Affiliations

Marius Anger[1] · **Petri Niemelä[1]** · **Kiril Cheremetiev[1]** · **Bruce Clayhills[1]** ·
Anton Fetzer[1] · **Ville Lundén[1]** · **Markus Hiltunen[1]** · **Tomi Kärkkäinen[1]** ·
M. Mayank[1] · **Lucile Turc[2]** · **Adnane Osmane[2]** · **Minna Palmroth[2,3]** ·
Emilia Kilpua[2] · **Philipp Oleynik[4]** · **Rami Vainio[4]** · **Pasi Virtanen[4]** ·
Petri Toivanen[3] · **Pekka Janhunen[3]** · **David Fischer[5]** ·
Guillaume Le Bonhomme[1] · **Andris Slavinskis[6]** · **Jaan Praks[1]**

✉ M. Anger
marius.anger@aalto.fi

P. Niemelä
petri.niemela@aalto.fi

K. Cheremetiev
kiril.cheremetiev@aalto.fi

B. Clayhills
bruce.clayhills@aalto.fi

A. Fetzer
anton.fetzer@aalto.fi

V. Lundén
ville.lunden@aalto.fi

M. Hiltunen
markus.hiltunen@aalto.fi

T. Kärkkäinen
tomi.karkkainen@aalto.fi

M. Mayank
mayank@aalto.fi

L. Turc
lucile.turc@helsinki.fi

A. Osmane
adnane.osmane@helsinki.fi

M. Palmroth
minna.palmroth@helsinki.fi

E. Kilpua
Emilia.Kilpua@helsinki.fi

P. Oleynik
philipp.oleynik@utu.fi

R. Vainio
rami.vainio@utu.fi

P. Virtanen
pakavir@utu.fi

P. Toivanen
petri.toivanen@fmi.fi

P. Janhunen
pekka.janhunen@fmi.fi

D. Fischer
david.fischer@oeaw.ac.at

G. Le Bonhomme
lebonhommeguillaume@gmail.com

A. Slavinskis
andris.slavinskis@ut.ee

J. Praks
jaan.praks@aalto.fi

1   Department of Electronics and Nanoengineering, Aalto University, Maarintie 8, Espoo, 02150, Finland

2   University of Helsinki, P.O. Box 68, Helsinki, FI-00014, Finland

3   Finnish Meteorological Institute, P.O. Box 503, Helsinki, FI-00101, Finland

4   Department of Physics and Astronomy, University of Turku, Vesilinnantie 5, Turku, 20014, Finland

5   Space Research Institute, Austrian Academy of Sciences, Schmiedlstraße 6, Graz, A-8042, Austria

6   Space Technology Department, Tartu Observatory, University of Tartu, Observatooriumi 1, Tõravere, Tartumaa, 61602, Estonia